

Study on the controlled self-assembly of magnetic nanostructures using neutron scattering

Sanctioned Order No. & Date: UDCSR/MUM/AO/CRS-M-186/12/508 Dated. 27-11-2012

Progress report of 2013-2016

(Complete report of the project)

**Principal Investigator: Dr. P. Deb,
Associate Professor
Department of Physics
Tezpur University (Central University)
Tezpur-784028, Assam**

**Principal Collaborator: Dr. Debasis Sen
Scientific Officer
Solid State Physics Division
Bhabha Atomic Research Centre
Mumbai-400085
India**

UGC-DAE CONSORTIUM FOR SCIENTIFIC RESEARCH MUMBAI CENTRE

R-5 SHED, B.A.R.C., MUMBAI-400085

A. Assembling magnetic nanoparticles in mesoporous silica for achieving high MRI contrast efficiency

1. Introduction

Designing of magnetic nanoparticle clusters with defined shape and compact structure has attracted lot of research attentions in recent time. This is due to their easy magnetic manipulation, high surface area, and multifunctional properties in comparison to the comprising individual nanoparticles [1-3]. However, many challenges are there in developing nanoparticle clusters with prolong stability and controlled morphology. In addition, it is necessary that the clusters have to retain the superparamagnetic property of the individual nanoparticles. Assembly formation of magnetic nanoparticles on a host material of nano to sub-micron size with inherent stability is a convincing solution for this, but prevailing condition is that individual magnetic nanoparticles need to be separated physically from each other. Mesoporous silica structures with diverge morphologies have shown tremendous opportunities in this direction. Their high stability, high bio-compatibility, versatility with respect to surface functionalization, and most importantly their versatile porous networks and labelling with wide range of functional molecules make them a suitable host material for fabrication of functional magnetic nanoparticles organizations [4].

In most of the works, silica was employed as the shell material for covering clusters of magnetic nanoparticles, while in some cases silica was employed as the core material on which magnetic nanoparticles are attached. However, in these types of structures either core or shell part of the silica spheres remains unused. For example, the sonication of $\text{Fe}(\text{CO})_5$ solutions in decalin containing silica particles resulted in structures composed of iron oxide nanoparticles heterogeneously grafted onto the silica spheres [5]. Another alternative strategy showed the coating of silica spheres with layers of iron compounds based on the forced hydrolysis of iron (III) acetylacetonate solutions containing the silica cores and a surfactant [6]. The coating of silica spheres with layers of preformed magnetite (Fe_3O_4) nanoparticles using a heterocoagulation process facilitated by charging the silica surface through the addition of a polyelectrolyte film has been also reported, although this method produced rough coatings [7]. In spite of this, many works are there, where clusters of magnetic nanoparticles were entrapped successfully inside silica spheres [8-9]. In contrast, this works demonstrates a mesoporous silica supported dense assembly structure of iron oxide nanoparticles, where, nanoparticles are not only placed on the surface of the silica spheres, but also get entrapped inside the silica spheres. A facile approach was employed for developing this structure, where the nanoparticles are homogeneously distributed all over the silica spheres. The method is based on solvent evaporation mediated entrapment mechanism at the hydrophobic-hydrophilic interface, which does not require any complicated surface functionalization steps.

The developed magnetic systems can find tremendous potential in biomedical field and the process observed is even interesting for developing new silica composite magnetic materials.

2. Results and discussion

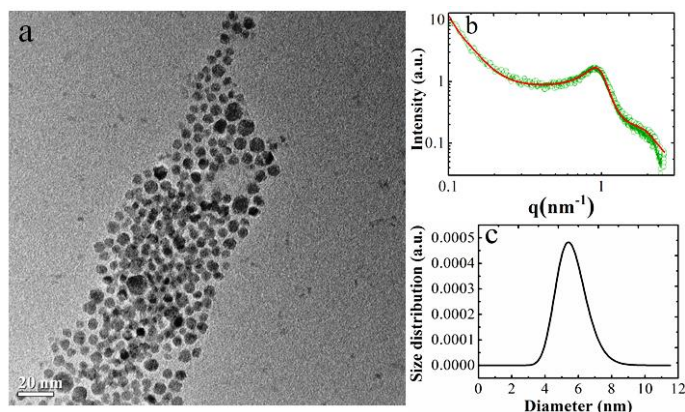


Fig. 1 TEM image (a) Fitted Small angle x-ray scattering profile in double logarithmic scale (b) and size distribution plot obtained from the fitting of SAXS profile of the iron oxide nanoparticles.

The TEM image shows a uniform distribution of the nanoparticles without any agglomeration characteristic. The SAXS profile in double logarithmic scale shows a peak at around q value of 0.1 nm^{-1} , signifying uniform ordering among the nanoparticles. The profile has been best fitted using the spherical form factor and hard sphere structure factor models and shows that the ordering parameter is nothing but the interparticle spacing of around 6.4 nm. The log-normal size distribution function has been used to fit the profile, which showed the median diameter of around 5 nm. The observed uniform separation among the nanoparticles is obviously due to the thick and effective oleic acid capping over them.

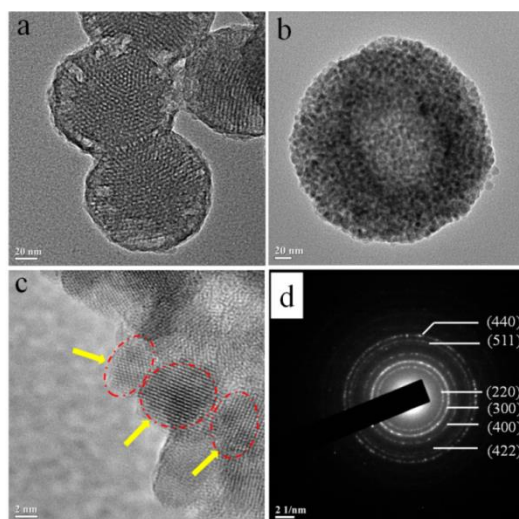


Fig. 2 TEM images of the mesoporous silica spheres S1 (a) iron oxide nanoparticles loaded silica spheres, S1@IO, (b) HRTEM of the S1@IO samples showing individual nanoparticles (c) and (d) the SAED of the S1@IO.

TEM images of the silica spheres before and after nanoparticles entrapment are shown in the Fig. 2(a) and (b) respectively. It is evident that the silica spheres with hexagonally packed straight pores have been densely filled up by the nanoparticles. No separate aggregation of the nanoparticles outside the silica spheres is observed. The TEM image in the Fig. 2c shows the entrapped iron oxide nanoparticles in the silica matrix clearly. The SAED pattern taken in the magnetic assembly system shows the characteristic diffraction rings of face center cubic structure of maghemite (JCPDS Card 39-1346).

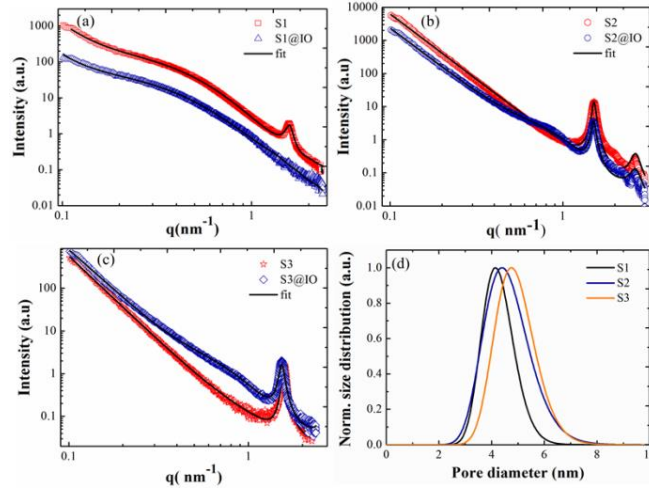
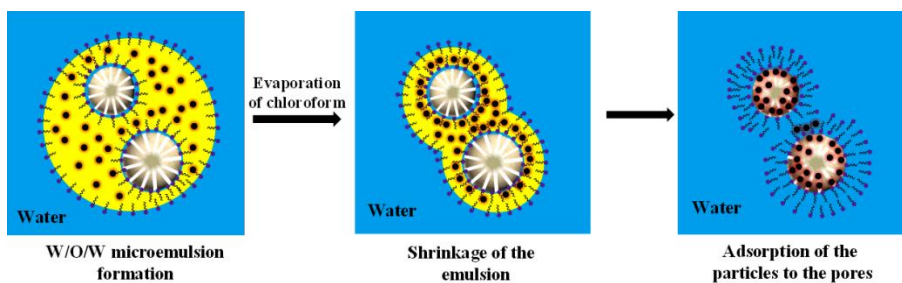


Fig. 3 Fitted SAXS profiles (in double logarithmic scale) of the three silica systems along with those after nanoparticles conjugations, (a) S1 and S1@IO, (b) S2 and S2@IO, (c) S3 and S3@IO and (d) shows the pore size distribution plots of the S1, S2 and S3 samples obtained from the respective SAXS profile fittings.

Effective scattering intensity for the S1 sample can be considered as the cumulative scattering contributions from three components, i.e., $I(q) = I_1(q) + I_2(q) + I_3(q)$, where, I_1 is the scattering intensity because of the presence of the correlated pores, I_2 is the scattering contribution from the whole silica grain and I_3 is the scattering contribution from a planar structure comprising of the multilayers of straight pores inside the spherical grain. However, for S2 and S3 samples, this third contribution has not been considered as this particular contribution remains absent owing to the absence continuity of the walls of the straight pore channels. ‘ q ’ is the scattering vector.

3. Mechanism of entrapment



Scheme 1 Schematic showing the entrapment mechanism of the nanoparticles in the mesoporous silica.

When both the solutions, i.e. the nanoparticles in chloroform and the suspension of silica spheres with CTAB were mixed, an emulsion was formed. The formed emulsion is basically of chloroform droplets dispersed in water phase and which are stabilized by the surfactant CTAB. The oleic acid capped nanoparticles are dispersed in chloroform phase. As soon as the evaporation of the chloroform starts, hydrophobic nanoparticles are bound to be adsorbed inside the pores of the silica spheres due to the continuous shrinkage of the hydrophobic environment. The hydrophobic interaction between the particles and the carbon chain of CTAB molecules also favours this adsorption process. As the evaporation process of the chloroform continues, nanoparticles are getting more and more entrapped to the pores of the silica spheres and even enter into the pores of the silica. CTAB molecules used for stabilizing the emulsion droplets envelope the clusters suddenly after completion of the evaporation process.

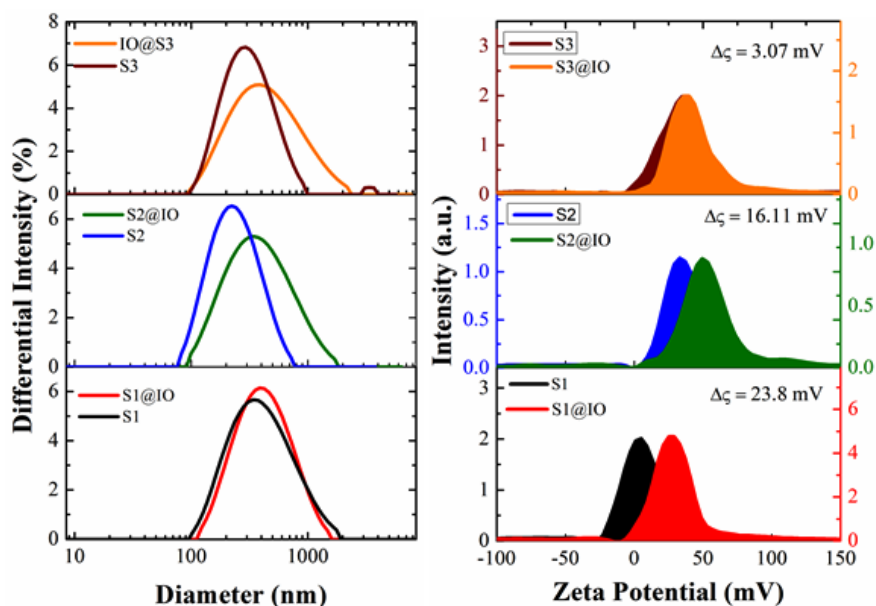


Fig. 4 Comparative size distribution plots from DLS and the comparative Zeta potential plots of the three silica systems and their respective nanoparticles composite samples.

Table 1: Table showing the mean particle sizes, polydispersity indices, Zeta potentials of all the three silica samples and silica-nanoparticles conjugate samples.

Samples	PDI	Mean Particle size (nm)	Zeta Potential (mV)	Difference in Zeta Potential (mV)
S1	0.266	350	4.0	23.1
S1@IO	0.233	401	27.1	
S2	0.224	221	33.0	17.62
S2@IO	0.269	345	50.62	
S3	0.217	283	35.01	3.42
S3@IO	0.251	383	38.43	

DLS measurements show the lower value of the polydispersity index for the nanoparticles loaded silica samples than that of the pure silica system (S1). However, for the other two silica samples it is observed to be increased after nanoparticles conjugation (shown in the Table 1 and Figure 4), which is due to the non-uniformity of the composite structures unlike the first sample. The mean hydrodynamic sizes of the silica-nanoparticle composite samples in all the three cases are observed to be increased. It is also seen that the increment of the hydrodynamic size for the later two samples are noticeable and the reason behind this could be the same, i.e., morphological non-uniformity of these two samples. On the other hand, the measurement of Zeta potential values shows that for the assembly system the value of the Zeta potential is increased significantly from the pure silica system and for the other two systems this difference decreases gradually (shown in the Table 1). The increment of the Zeta potential is due to the enhanced stability of the particles resulted from the uniform enveloping of the CTAB molecules over it during the process of nanoparticles entrapment. Since, for the other two samples this enveloping process is not happening properly and separate aggregations of the nanoparticles are formed outside the silica, hence less differences in Zeta potential values before and after nanoparticles conjugation are observed. However, it is noticeable that for the second system (S2) the difference of the Zeta potentials values is not very small, which can be correlated to the partial loading of the particles to silica as mentioned in the earlier discussions. Though, the stability of the nanoparticles loaded silica spheres improved from the pure silica spheres due to the presence of CTAB molecules, but after a single washing cycle with water it lost its stability with reduction of the zeta potential to +8.00 mV. Moreover, the precipitate was dispersed easily in hydrophobic solvents, which is surely due to the removal of the loosely bound CTAB molecules and exposure of the oleic acid capped hydrophobic particles.

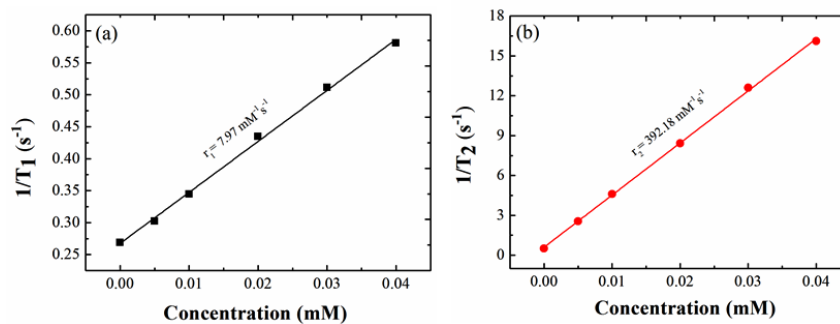


Fig. 5 r_1 and r_2 relaxivity plots of the S1@IO sample are shown in figures (a) and (b) respectively.

Fig. 5 shows the r_1 and r_2 relaxivity plots of the $\gamma\text{-Fe}_2\text{O}_3$ nanoparticles loaded silica spheres (S1@IO). The system also shows high value of r_2 relaxivity in comparison to $\gamma\text{-Fe}_2\text{O}_3$ nanoparticles. The r_1 relaxivity value is also good, but it cannot be said as an acceptable T_1 contrast agent due to very high value of the ratio r_2/r_1 . The observed higher value of T_2 relaxivity can be again justified due to the dense assembly formation of the nanoparticles. Here, also the comparison of relaxivity values can be done with that of CTAB stabilized iron oxide particles in the first case, because the basic size and composition of the particles are same in both cases.

4. Conclusion

The evaporation of solvent is realized to be helpful for obtaining dense assembly of magnetic nanoparticles in Mesoporous silica spheres. The nanoparticles get entrapped to the pores effectively even after having higher size of the particles than the pore diameter, which is due to the triggering force on the particles to pores as the result of solvent evaporation. However, the nature of the pore correlation effect on this mechanism. In this study, it is observed that mesoporous silica only with straight pores have filled up the nanoparticles, while the silica with curved and twisted pores could not. SAXS profiles also supported the evidences obtained from the TEM images on this argument. Zeta potential and DLS measurements also supported the same by showing significant increase after nanoparticles entrapment. Magnetic properties measurements have showed retaining of the superparamagnetic property of the nanoparticles even after dense assembly formation. This can be justified by the fact that, effectively there is less interparticle interaction due to spacing between the individual assemblies even though particles are densely assembled inside the silica spheres. Therefore, the developed assembly system can find potential application in the biomedical applications.

B. Varying collective magnetic properties of secondary nanostructures with differential spatial ordering and magnetic easy axis orientation

1. Introduction

Modification in the moment relaxation dynamics due to the influence of dipolar interaction is still a controversial issue. Dormann-Bessais-Fiorani (DBF) model is an acceptable model which showed the slowing of moment relaxation time with the increasing strength of dipolar interaction [10, 11]. Most of the experimental data were well explained by this model. Their assumption was based on the effect of a dynamic interaction field, where the particles' blocked and unblocked states were assumed in the experimental time window. Later DBF model was reconfirmed by the Monte Carlo based simulation, where it was observed that the effective anisotropy energy barrier increases due to the formation of an increasing number of small energy barriers caused by the reduction of anisotropy barriers as the local dipolar fields increase [12]. In contrast, Morup model showed faster relaxation time due to interparticle interaction [13]. Morup model put forwarded a "flip" process, where, it was assumed that the magnetic moment of a particle spends most of the time close to its easy direction. But, this assumption is not acceptable at high temperature, i.e. in the unblocked state, because in the unblocked state the probability of finding magnetic spins outside of the minima is appreciable. It is worth mentionable that both of these phenomenological models have considered only the random distribution of the magnetic easy axes, but not any partial alignment of easy axes or particular geometry of the assemblies. Influence of partial alignment of magnetic easy axes on the modification of magnetic properties like, coercivity and remanence was shown [14]. However, these studies have not shown the effect of easy axes alignment on relaxation dynamics or on blocking temperature. It is very much probable that the alignment of magnetic easy axes can effect on blocking temperature too through variation in the self-produced demagnetizing field.

Demagnetizing field is a homogeneous field originating from the dipolar interaction, whose strength depends on the average ensemble magnetization and sample shape. In an organization of arbitrary shape demagnetizing field depends on the particles positions relative to the sample boundaries [15]. Along with, the partial alignment of the magnetic easy axes is another factor for influencing the strength of demagnetizing field. For instance, organization of single-domain magnetic nanoparticles with aligned easy axes will hardly show demagnetizing effect rather than showing magnetizing effect. Therefore, in the calculation for relaxation time for interacting magnetic nanoparticles the contribution of demagnetizing field along with the dynamic dipolar field has to be considered to have an acceptable solution of this problem. This approach was attempted by theoretical approach, but so far we know no reports have shown this through experimental data.

Many reports are there, where the dipolar interaction among magnetic nanoparticles was tuned using non-magnetic capping molecules or isolating nanoparticles inside some non-magnetic cages [16]. There are also some other routes, where, volume fraction of magnetic nanoparticles is

varied in non-magnetic matrixes for controlling interparticle spacing [17]. However, in such systems it is not feasible to control on spatial ordering and easy axes orientation at the same time. Based on the clusters' size or magnetic volume fraction on non-magnetic matrix, only some tentative measurement of interparticle spacing can be estimated which is related to the observed magnetic properties.

In contrast, this work has considered the effect of spatial arrangement and orientation of magnetic easy axes of iron oxide nanoparticles together on demagnetizing interaction and hence on the observed collective magnetic properties. In this regard, three systems have been developed, namely, (i) $\text{IO}_{\text{NPs}}@OA$; an assembly of iron oxide nanoparticles, where, nanoparticles are separated by a measurable spacing, (ii) $\text{IO}_{\text{agg}}@CTAB$; an network aggregation of the same nanoparticles, where, particles are situated side by side at the closest distance from each other and (iii) $\text{IO}_{\text{NPCs}}@PAA$; identical clusters of the same nanoparticles, where the particles are at some measurable separation, but much smaller than in the assembly system. Based on the preparation strategies of these three systems and the intrinsic magnetic nature of the nanoparticles, different ground state of magnetic spin structures have been achieved, which have been related to the collective magnetic properties. Since, all the three systems have been developed from the same batch of primitive nanoparticles, so the effect of size distribution is not considered in the study.

2. Results and discussion

2.1 Organizations and phase of iron oxide nanoparticles

Oleic acid capped iron oxide nanoparticles were synthesized by oxidation of ferrous salt in presence of oleic acid. TEM (shown in Fig. 1a) shows the uniform distribution of the synthesized nanoparticles with average size 5 ± 2 nm. The average interparticle spacing is found to be 5.8 nm. So-prepared nanoparticles were then functionalized with a microemulsion method using CTAB (Cetyltrimethylammonium bromide), which resulted in a network aggregation of the nanoparticles with interconnected chain morphology (shown in Fig. 1b) due to the fast solvent (chloroform) evaporation. This system of hydrophilic nanoparticles was further treated with the polyelectrolyte PAA (Polyacrylic acid) for clustering purpose (shown in Fig. 1c). These three steps methods are elaborated in the online supplementary information (ES1). Wrapping nature of the polymer is thought to be responsible for the formation of separate clusters. TEM results reveal that in the cluster system (shown in the inset of Fig.1c) a measurable interparticle spacing (5.6 nm) among the nanoparticles has been achieved unlike the aggregate system ($\text{IO}_{\text{agg}}@CTAB$).

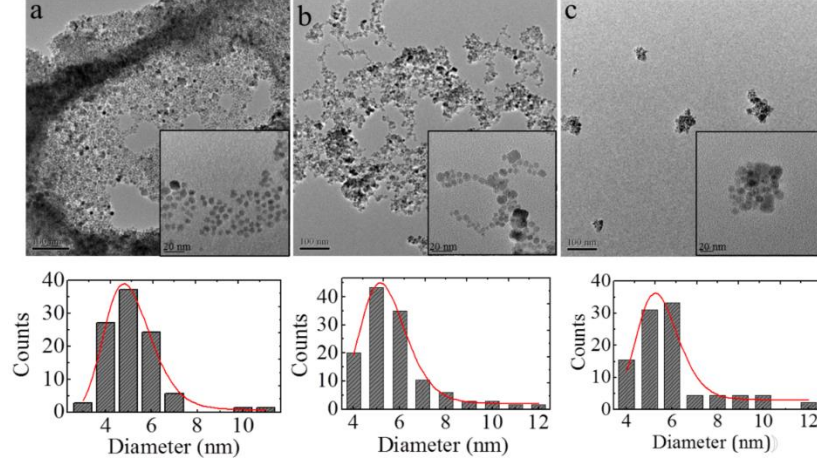


Fig.1. TEM images of $\text{IO}_{\text{NPs}}@OA$ (a), $\text{IO}_{\text{agg}}@CTAB$ (b) and $\text{IO}_{\text{NPCs}}@PAA$ (c) systems. The inset figures show the respective magnified images. Size distribution plots of the respective system are shown below.

2.2 Small angle scattering based structural investigations

To access the overall structural in-formations in the whole length scales ranging from individual nanoparticle dimension to the nano clusters size both SAXS and SANS have been used. In order to obtain the size distribution of the basic particles, the obtained SAXS scattering intensity profile has been fitted with the scattering model of a polydisperse ensemble of interacting spherical particles. The observed intensity can be approximated as

$$I(q) = C \left(\int_0^{\infty} \rho(R) R^6 F^2(q, R) dR \right) S(q, R') \quad (1)$$

where, C is the scale factor that depends on the scattering density contrast and the number density. $\rho(R)$ represents the radial size distribution function, $F(q, R)$ is the form factor of a particle with radius R and $S(q, R')$ represents the interparticle structure factor with the effective interparticle distance $2R'$. The form factor $F(q, R)$ of a spherical scatterer with radius R is given by

$$F(q, R) = 3[\sin(qR) - qR\cos(qR)]/(qR)^3 \quad (2)$$

The size distribution $\rho(R)dR$ represents the probability of finding a particle with radius R to $R + dR$ and has been assumed as log normal distribution function.

$$\rho(R) = \frac{1}{\sigma R \sqrt{2\pi}} \exp \left[-\frac{(\ln(R) - \ln(\mu))^2}{2\sigma^2} \right] \quad (3)$$

where, σ and μ represent the polydispersity index and median of the radius distribution respectively.

The nature of the profile at low q regime is determined by the nature of structure factor. For an attractive potential, the intensity at low q increases because of the formation of aggregated structure of the particles. In low q region of the SAXS profiles, the power law dependence of $I(q)$ on q (i.e., linear relation in double logarithmic scale) and with non-integer exponent of power law indicate fractal like morphologies in all the three systems, irrespective of assembling, aggregation and reassembling. In reality, power law scattering is manifested in a limited q range determined by upper and lower cut-off lengths between which the system behaves as a fractal.

So, scattering curves are modelled using the form factor of a polydisperse spheres (subunit or monomer) and a mass fractal structure factor

$$S(q, r_o) = 1 + \frac{D}{r_o^D} \int_0^\infty R^{D-3} h(r, \xi) \frac{\sin(qr)}{(qr)} r^2 dr \quad (4)$$

with the fractal dimension, D , the radius of the monomer, r_o , the cut-off function $h(r, \xi)$ and ξ , cut-off length for fractal correlation. It has been found that, $S(q, R')$ corresponding to $h(r, \xi)$ of either, exponential cut-off or Gaussian cut-off represents well the present data,

$$\text{Gaussian cut-off, } h_{Gauss}(r, \xi) = \exp\left[-\left(\frac{r}{\xi}\right)^2\right] \quad (5)$$

$$\text{and exponential cut-off, } h_{Exp}(r, \xi) = \exp\left[-\left(\frac{r}{\xi}\right)^1\right] \quad (6)$$

Fig.2a shows the transmission corrected scattered intensity profiles along with fitted curves. The fitted parameters such as fractal dimensions (D_m) of the systems and their basic subunit size (μ), polydispersity index (σ) and the approximate interparticle distance ($2r$) for all three systems are listed in the table 1. The SAXS curves for the $\text{IO}_{\text{NPs}}@ \text{OA}$ and $\text{IO}_{\text{NPCs}}@ \text{PAA}$ are fitted with two contributions; (i) basic nanoparticles with fractal morphology and (ii) a very small length scale (~ 2 nm) which could be due to oleic acid capping over the nanoparticles. Fig.2c shows the size distribution profiles of the subunits which is almost corroborating with the same obtained from TEM (size distribution histogram is shown in Fig.1). Also, the interparticle spacing measured from the high magnification TEM images are corroborating well with the SAXS results. It is worth mentioning here that the interparticle spacing distribution profiles are approximated from the average interparticle spacing and width of the particle size distribution obtained from SAXS. However, the slight dissimilarities in the trend of size distribution, polydispersity index and mean size can be attributed to the fact that the applied scattering tools are believed to give the overall structural informations about the system, while TEM provides the selective informations based on the region of interest. In this scenario, it will be more reliable for the explanation of magnetic properties on the basis of structural information obtained from scattering data, as the measured magnetic properties are the collective properties of the systems.

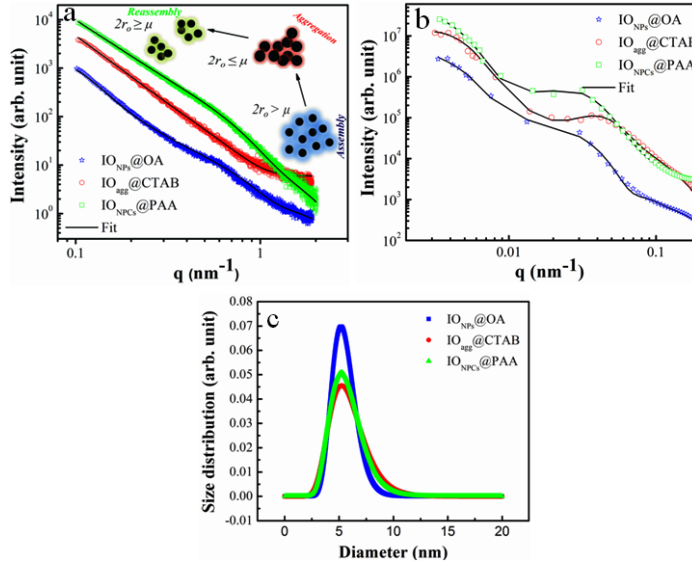


Fig.2 (a) SAXS and (b) SANS profiles in double logarithmic scale (Solid lines represent the fitted curves) (c) is the lognormal size distributions nanoparticles obtained from SAXS data.

Table 1: Estimated structural parameters from SAXS and HRTEM.

System	Fractal dimension (D_m)	Median size (μ) of the NPs (nm)		Polydispersity index (σ)		Interparticle distance ($2r_o$) (nm)	
		HRTEM	SAXS	HRTEM	SAXS	HRTEM	SAXS
IO _{NPs} @OA	2.43 ± 0.01	5.0	5.40 ± 0.02	0.206	0.20 ± 0.01	6.3	5.8
IO _{agg} @CTAB	2.59 ± 0.01	5.3	5.68 ± 0.03	0.186	0.28 ± 0.01	4.9	4.8
IO _{NPCs} @PAA	2.39 ± 0.01	5.4	5.58 ± 0.02	0.169	0.26 ± 0.01	5.5	5.6

It should be emphasized that, since all the three systems have been obtained from the same batch of nanoparticles, the particle size distributions should be same. This is confirmed from the observed similarity of size distribution plots (Log-normal distribution) estimated from the TEM images and overlapping of the same obtained from the analysis of SAXS (small angle X-ray scattering) data. Another observation is the retaining of the same structural phase of the nanoparticles, which has been confirmed from the analysis of Raman spectra (shown in figure 3). Raman spectra show the characteristic peaks of maghemite (γ -Fe₂O₃) phase for the iron oxide nanoparticles in all three systems. Three distinct peaks around 350 cm⁻¹, 500 cm⁻¹ and 670 cm⁻¹ are assigned to the E_g, T_{2g} and A_{1g} vibration modes of $O_h^7(Fd3m)$ space group of maghemite. As Raman spectroscopy was performed at extremely low laser power (0.01 mW) and with short

exposure time, the laser induced phase transformation of magnetite to maghemite can be discarded here. So, the observed phase can be argued as the intrinsic phase of the nanoparticles.

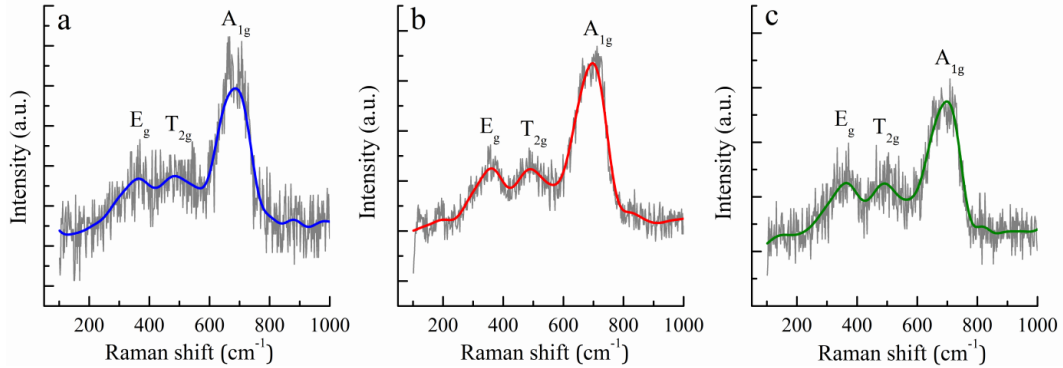


Fig. 3. Raman spectra of (a) $\text{IO}_{\text{NPs}}@ \text{OA}$, (b) $\text{IO}_{\text{agg}}@ \text{CTAB}$ and (c) $\text{IO}_{\text{NPCs}}@ \text{PAA}$ systems. Blue, red and green lines are showing the FFT smoothing.

2.3 Effect of particles arrangement on interparticle interaction strength

As size and phase of primary nanoparticles are retained in all the three systems, the modification in collective magnetic properties has to be solely dependent on the nature and strength of interparticle interaction in three systems. To probe the nature of interaction among the constituent nanoparticles and its comparative strength in three systems, isothermal remanent magnetization (IRM) and direct current demagnetization (DCD) measurements were carried out. For a system of non-interacting magnetic nanoparticles with uniaxial anisotropy these two field dependent remanent magnetizations are related by the Wohlfarth equation (7).

$$\delta M = M_{\text{DCD}} - (1 - 2M_{\text{IRM}}) \quad (7)$$

where, M_{IRM} and M_{DCD} are normalized remanent magnetizations. When, $\delta M = 0$, it signifies that there is no interparticle interaction in the system, while negative and positive values of it attribute to predominant demagnetizing and magnetizing types of interactions respectively. The δM plots showed in the figure 4 exhibit negative values of δM for all the three systems signify the predominant demagnetizing type of interaction among the particles. However, there are significant differences among the interaction strengths for the three systems. For the assembly system δM is observed minimum and for the cluster system it is seen maximum, signifying that the strength of dipolar interaction among the nanoparticles in the assembly system is weak, while in the cluster system it attains the maximum. The comparative dipolar interaction strength can be directly related to the average interparticle spacing among the nanoparticles. For the first two systems, the interaction strength is observed to be increased with decreasing average interparticle spacing, which is obvious. However, for the cluster system the obtained maximum interaction strength from δM plot is something unusual, as in this system, unlike the aggregate system particles are not in direct contact. TEM images clearly show some measurable interparticle spacing among the particles inside the cluster (shown in the Fig. 1f). Random orientation of

magnetic easy axes of the particles in the cluster system and possible preferential alignment of easy axes in the aggregate system could be the reason, due to which the cluster system shows the stronger dipolar interaction strength than the aggregate system. This is also confirmed from the calculated values of H_{in} (shown in Table 1) for the three systems, which suggests the strongest demagnetizing interaction for the cluster system.

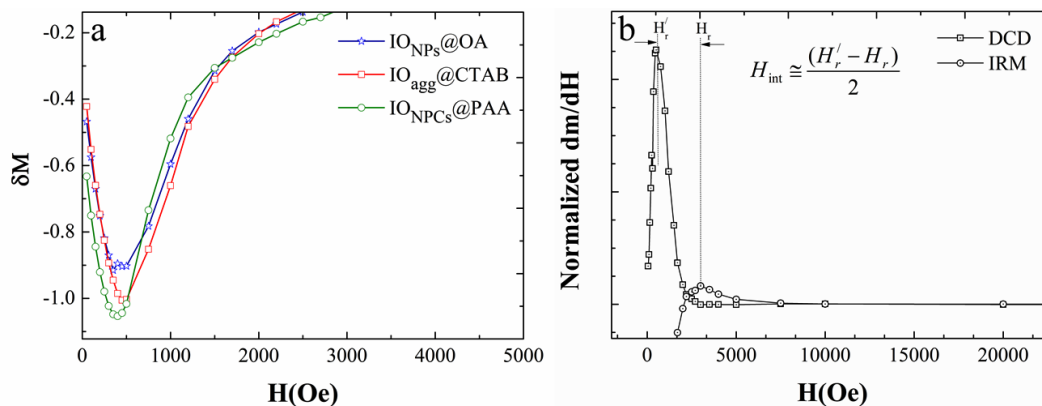


Fig. 4. (a) Comparative δM plots of the three systems and (b) shows the derivatives of m_{IRM} and m_{DCD} against magnetic field for the $\text{IO}_{\text{NPs}}@OA$ sample. The inset of Fig. b shows the equation for H_{int} calculation, where, H'_r and H_r represent the peaks positions of the derivatives plots of IRM and DCD respectively.

The possibility of partial alignment and random distribution of nanoparticles' easy axes in the aggregate system and cluster systems respectively, can be understood by revisiting the formation mechanisms of the three systems. Like the oleic acid capped nanoparticles in the assembly system, CTAB functionalized nanoparticles are also free to rotate in all directions during solvent evaporation. However, the difference is that, after CTAB functionalization, hydrophilic-hydrophilic interaction among the particles may promote different aggregation morphologies depending on the density of the nanoparticles. Here, the observed stacking aggregation morphology of CTAB stabilized nanoparticles is such an energetically favorable configuration, where stacking of the nanoparticles facilitates the alignment of easy axes. On the other hand, in the case of PAA treated system, nanoparticles are likely to be attached to the oriented carboxylate groups (COO^-). This oriented attachment never allows the free rotation of the particles during solvent evaporation. Hence, this process yields in some cluster morphology of nanoparticles with random orientation of easy axes. Similar to this system, the possibility of easy axes alignment in the primitive system is also very less as there due to steric hindrance nanoparticles are bound to separate from each other at measurable distances. Schematic shown in the Fig. 5 clarifies the demonstrated mechanism. For more clarification on it, a quantitative estimation on the degree of partial alignment of easy axes is done using the FC magnetization values of three systems. The degree of partial alignment of easy axes in three systems can be estimated from the equation (2).

$$M_{\text{FC}}^{\text{align}} / M_{\text{FC}} = 1 + \alpha(3\cos^2\beta - 1) \quad (8)$$

where, $M_{\text{FC}}^{\text{align}}$ is the FC magnetization at the lowest temperature (10 K) for the system with aligned easy axes, M_{FC} is the same, but for the system with random orientation of easy axis, β is the average angle between applied magnetic field and magnetic easy axes and α is the fraction of nanoparticles with aligned easy axis. If the entire easy axes are randomly oriented, $\alpha = 0$ and hence $M_{\text{FC}}^{\text{align}} / M_{\text{FC}} = 1$. Applying this equation to the three systems, the ratios $M_{\text{FC}}^{\text{agg}} / M_{\text{FC,NPs}}$ and $M_{\text{FC}}^{\text{NPCs}} / M_{\text{FC,NPs}}$ are obtained as 1.25 and 1.19 respectively. From this estimation it can be concluded that the partial alignment of easy axes in the aggregate system is higher than that in the cluster system.

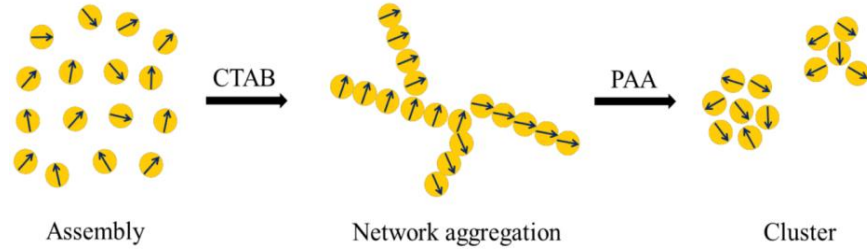


Fig. 5. Schematic presentation of three systems along with the easy axes orientations. The assembly system shows well separation among the particles with random orientation of easy axes. The aggregate shows physical contact among the nanoparticles with partial alignment while the cluster system shows random orientation of nanoparticles with some measurable spacing.

Thus, the change in easy axes' orientations along with the interparticle spacing of the nanoparticles in the three systems might be responsible for the observed variation in the dipolar interaction. Stacking of the nanoparticles with aligned easy axes in the aggregate system gives rise to positive or magnetizing type of dipolar interaction, while in the cluster system random orientation results for negative or demagnetizing type of dipolar interaction. For the assembly system, since nanoparticles with random easy axes are separated from each other at measurable distances, so it is not possible to create flux-closed loop like in the cluster system for resulting significant demagnetizing effect.

2.4 Energy barrier distributions

The effect of demagnetizing interaction on modifying the anisotropy energy barrier distributions is also critical. Fig.5 shows that for all the three systems the remanence is decreased in exponential way with the increase of temperature, which is usually expected for an assembly of single domain particles. However, the cluster system shows the fastest decay of the remanence

with increasing temperature. This could be again related to the fast magnetic reversal process due to the strongest demagnetizing interaction in the cluster system. The actual picture of energy barrier distributions is obtained only after proper investigation of the derivative plots. For non-interacting particles, the derivative plot of M_{TRM} with respect to temperature gives the estimation of anisotropy energy barrier distribution (equation 9).

$$f(E) \propto -\frac{dM_{TRM}}{dT} \quad (9)$$

Here, the derivative of M_{TRM} can be actually considered as the indication of energy barrier distribution, because role of interparticle interaction on ensemble of magnetic nanoparticles cannot be neglected. Therefore, the observed deviation of derivative plots from each other for the three systems can be used as the indication of modified energy barrier distribution. Fig.6 also shows that, the anisotropy energy barrier peak for the aggregate system is comparatively broader, while the other two systems show almost similar broadening. However, there is not any measurable difference in the center position of the peak maxima, which could be due to the similar basic size of the particles. The observed significant broadening of energy barrier distribution can be related to lowest demagnetizing effect in this system, which is also reflected on the measured coercivity and reduced remanence values.

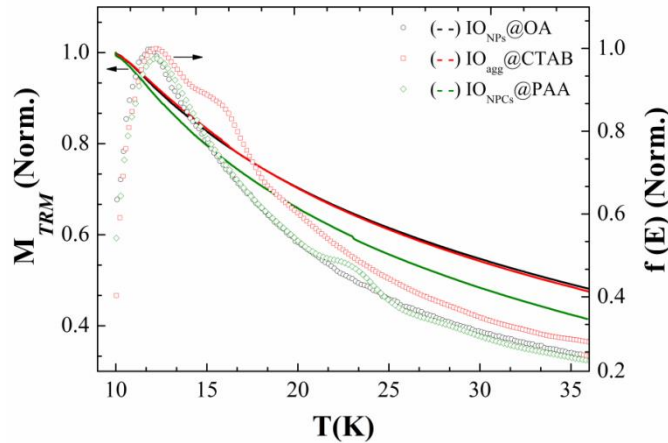


Fig 6. Thermoremanent magnetization (TRM) and the respective derivative plots of the three systems are shown in double y plots.

2.5 Coercivity and remanence

Fig.7 shows the temperature dependent M-H measurements of the three systems at four temperatures. Table2 shows the measured coercivity and reduced remanence values. Field dependent magnetization (M-H) measurements at room temperature as well as at low temperatures show the highest coercivity for the aggregate system and the lowest for the

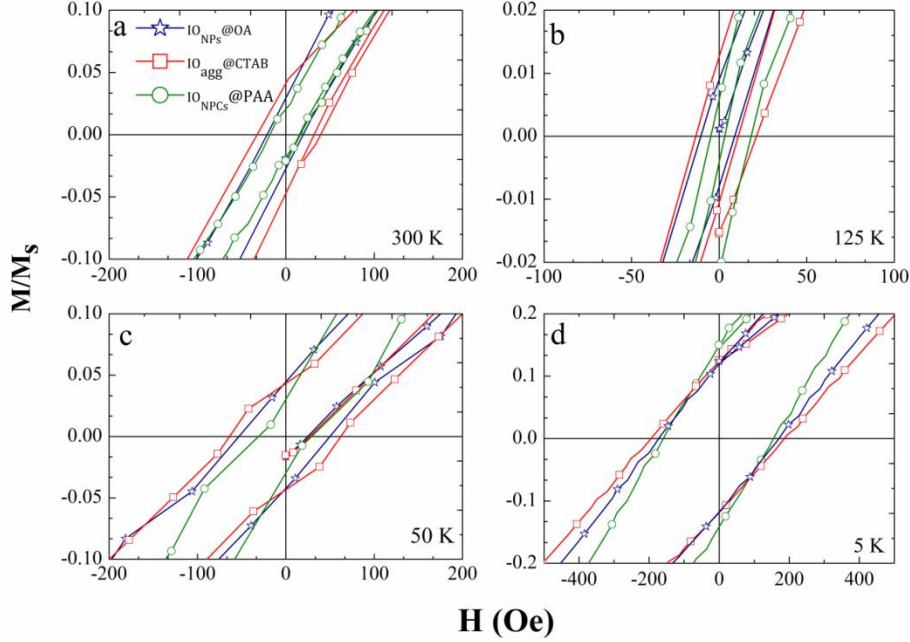


Fig. 7. M-H plots of the three systems showing coercivities and reduced remanences at temperatures (a) 300 K, (b) 125 K, (c) 50 K and (d) 5 K.

cluster system. However, coercivity values are observed to be increased with lowering the measurement temperature. The observed lowest value of the coercivity for the cluster system with the strongest dipolar interaction is expected as demagnetization character of dipolar interaction is likely to make the magnetic reversal process easier. But the same is not observed for the aggregate system as this system should show the lower value of coercivity in comparison to the assembly system. Anisotropic aggregation of the aggregate system results for the maximum coercivity due to the partial alignment of easy axes even after having the stronger dipolar interaction than the assembly system. Similar to the coercivity values reduced remanences are also showing the same trend for the three systems except at the measurement temperature 5 K. At this temperature, the cluster system shows the maximum reduced remanence value. At extremely low temperature, Zeeman energy (μH) can overcome thermal energy (kT), and therefore it is highly possible to rotate the individual clusters along the field direction for resulting higher remanence. Another observation is that at 125 K both coercivity and reduced remanence values are observed smaller than that observed at 300 K. This can be related to the Verwey transition of the iron oxide (magnetite composition) nanoparticles around this temperature. Since all three systems show the lowering of both coercivity and reduced remanence at this temperature, so it can be told that the strength of interparticle interaction has not any influence on Verwey transition of magnetite nanoparticles. The uniaxial anisotropy of the nanoparticles in all three systems has been confirmed from the observed lower value of reduced remanence than 0.5.

System	Coercivity H_c (Oe)				Reduced Remanence (M_r/M_s)				H_{in} (kOe)
	5 K	50 K	125 K	300 K	5 K	50 K	125 K	300K	
IO _{NPs} @OA	169.73	52.41	8.83	20.05	0.11	0.04	0.009	0.03	-2.4
IO _{agg} @CTAB	185.7	63.81	10.96	35.57	0.11	0.04	0.013	0.04	-1.9
IO _{NPCs} @PAA	155.35	30.22	3.24	19.41	0.14	0.03	0.006	0.02	-2.6

Table 2. Temperature dependent coercivities and reduced remanences and interaction field of all the three systems.

2.6 ZFC and FC magnetizations

Temperature dependent magnetization studies have been carried out using FC (field cooling) and ZFC (zero field cooling) protocols. All the three systems show the blocking temperatures well below the room temperature, which is a typical characteristic of superparamagnetic property (shown in Fig. 8). Moreover, the absence of any plateau like shape of the FC curves below blocking temperature implies that there is not any development of spin-glass state in any one of the systems.

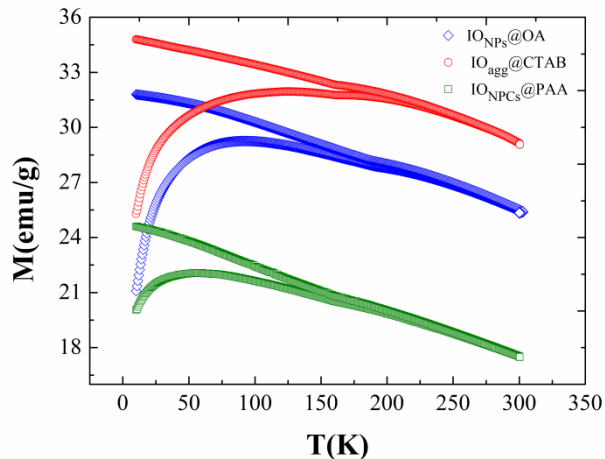


Fig. 8. M-T measurements (FC and ZFC) of the three systems with probe field 500 Oe.

The trend of the blocking temperature shifting with the trend of dipolar interaction strength is something unusual, as here the shifting of blocking temperature is observed to be shifted to lower temperature with the increase of dipolar strength (for the cluster system). Thus this does not follow the DBF model. But, it will be also wrong to conclude that the Morup model is followed here. Since the cluster system is not a continuous network of nanoparticles aggregation like the anisotropic aggregate and the primitive assembly systems, the average thermal energy required to make the collective spins free for thermal fluctuation could be minimum. More precisely, the observed reduced blocking temperature can be related to the easy magnetic reversal as the result

of strongest demagnetizing effect fascinated by closed packed random easy axes orientations in clusters. If the internal magnetic field in the formalism of DBF model is modified by contribution of demagnetizing field, then it could show the lowering of blocking temperature for the system with increasing the demagnetizing field strength. This could be the reason for shifting of the blocking temperature of the cluster system to the lowest value even after observing the strongest dipolar interaction. This can also be linked to the observed faster decay of remanence with temperature in TRM measurement as well as the lowest coercivity and reduced remanence in M-H measurements. Blocking temperatures calculated from Kneller plots (shown in the Fig.9) also show the same trend. The Weiss temperature θ obtained from the Curie-Weiss fits in the high temperature regions (shown in figure 10) show the maximum value (130 ± 3 K) for the aggregate and minimum for the cluster system (60 ± 2 K). The obtained trend of Weiss temperature also reflects the same trend that of the blocking temperatures. The maximum value of Weiss temperature for the aggregate system implies the higher degree of super-spin alignment. It is worthwhile to mention that the measured dipolar interaction form δM plot is the reflection of the magnetizing and demagnetizing characters which depends directly on the easy axes orientation and interparticle spacing. In the cluster system, though individual clusters are separated from each other, but within the clusters nanoparticles with random orientation of easy axes are compact enough for giving predominant negative dipolar interaction.

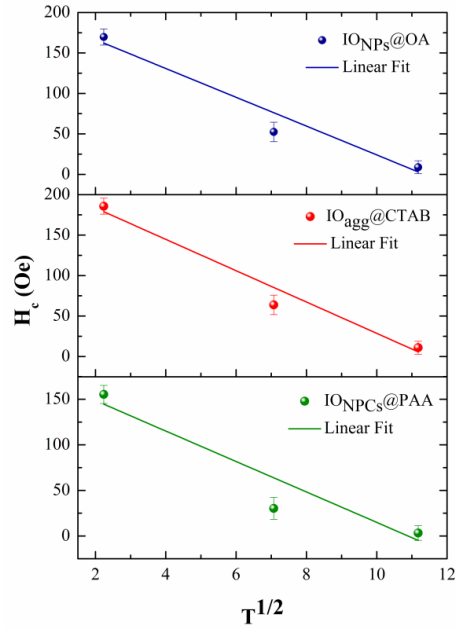


Fig.9. Kneller's plot for the three systems

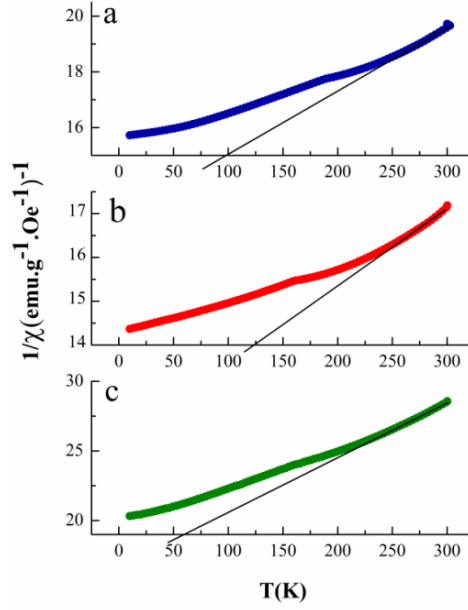


Fig. 10. Inverse susceptibility plots for the three systems (a) $\text{IO}_{\text{NPs}}@OA$ (b) $\text{IO}_{\text{agg}}@CTAB$ and (c) $\text{IO}_{\text{NPCs}}@PAA$. All the three plots imply the ferromagnetic ordering and which is obtained maximum for the aggregate system and lowest for the cluster system.

$$H_C = H_{C0} \left[1 - \left(\frac{T}{T_B} \right)^{1/2} \right] \quad (10)$$

Blocking temperature T_B has been also calculated using Kneller's equation (4), where, H_{C0} is the coercivity at absolute zero temperature and T_B is the blocking temperature. Table 2 shows the estimated values from the linear fitted plots. It is observed that the calculated T_B follows the same trend with T_{peak} obtained from M-T measurements.

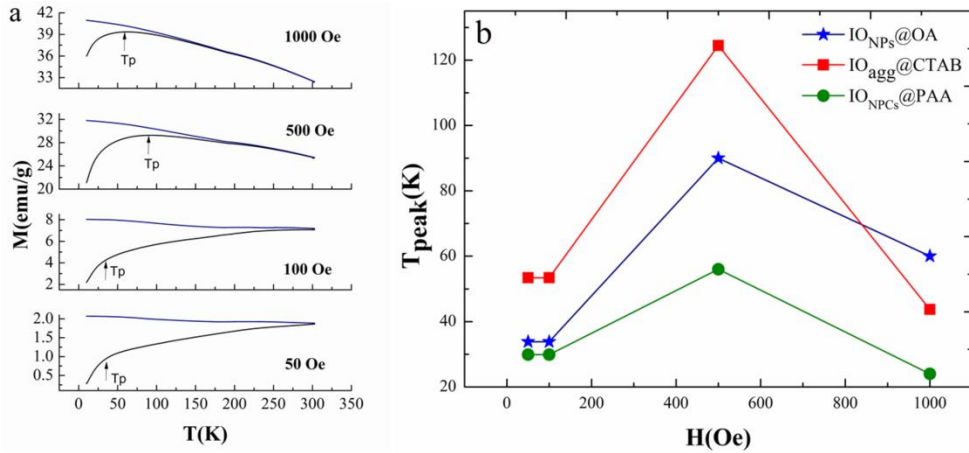


Fig. 11. (a) M-T measurements of $\text{IO}_{\text{NPs}}@OA$ at different field strengths and (b) shifting of T_{peak} with the applied probe field.

Fig.11 shows the field dependent M-T measurements as well as the shifting of peak temperature with the increasing probe field. The observed non-monotonic field dependence of ZFC peak temperature signifies the dominant effect of Zeeman energy (μH) over thermal energy (kT). The

decrement $M(T)$ curves with slower rate above the peak temperature than the prediction of Curie law further justifies that in all three cases Zeeman energy is much larger than the thermal energy, i.e, $\mu H \gg kT$. However, the usual trend of lower temperature shifting of T_{peak} is observed after the using of higher field. It is also observed that the peak height and sharpness of plot (T_{peak} vs H) for the aggregate system is higher in comparison to the other two samples. The sharper peak gives the evidence of the strongest Zeeman interaction energy which could be due the highest effective anisotropy energy resulted from the partial alignment of easy axes at the closest distance in the aggregate system.

2.7 FC memory effect

For FC memory study, the samples were cooled in presence of 500 Oe magnetic field from 300 K to 10 K with intermittent stopping for 1 hour each at 80 K, 60 K, 40 K and 20 K. After completion of the cooling process, the magnetization was measured with continuous warming upto 300 K. The reference curves were measured with the same procedure, only the cooling process was completed here without any intermittent stopping steps. Figure 12 shows the FC memory effect of the three systems. It is observed that $\text{IO}_{\text{NPs}}@OA$ system shows pronounced three steps memory effect, while for the other two systems all steps are not so clear. However, $\text{IO}_{\text{agg}}@CTAB$ system shows the memorizing of the first two steps similar to the $\text{IO}_{\text{NPs}}@OA$, for $\text{IO}_{\text{NPCs}}@PAA$ the memory steps are observed significantly weak. To have a firm conclusion on it, the derivatives of FC warming have been plotted, which has clarified the same. Since primary nanoparticles in all three systems are same, the effect of size distribution can be discarded for the observed variation in FC memory effect. In this situation, the observed trend of FC memory effect for the three systems should be dependent on the variation interparticle interaction strength. It is known that the FC memory effect is just the reflection of distribution of relaxation time in an ensemble of magnetic nanoparticles. So, in absence of any interaction also memory effect can be observed. Even dipolar interaction is identified as the reason for lowering of the FC memory effect.

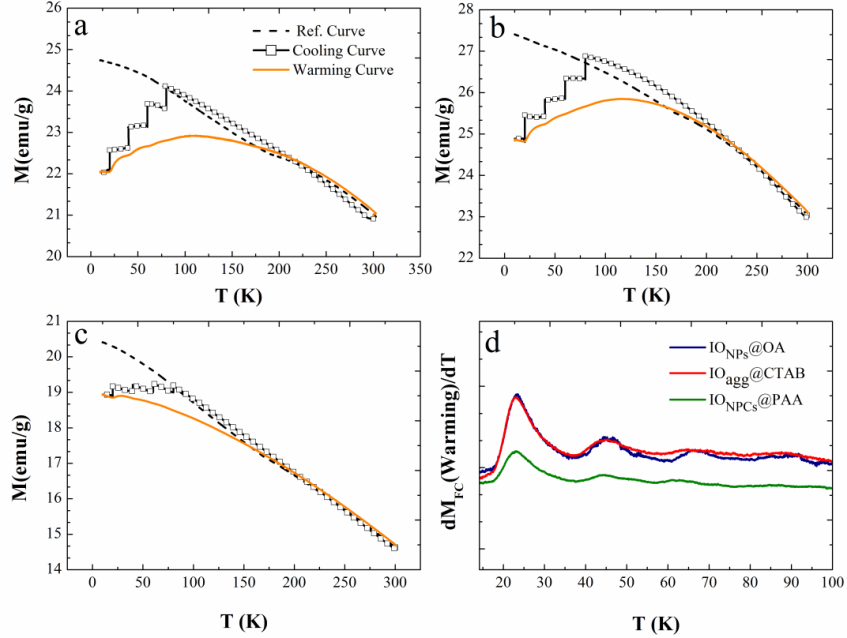


Fig. 12. (a-c) FC memory effect for the three systems and (d) shows the temperature derivative of FC warming curves.

In some cases, strong dipolar interaction makes the collective spin dynamics of a system of magnetic nanoparticles more complicated for resulting enhanced memory effect. Thus, the effect of dipolar interaction on FC memory effect is still under controversy. But, we have observed the suppression of memory effect with increasing dipolar interaction for these three systems. For the primitive assembly system, it is observed maximum, where, δM plot shows the least dipolar interaction, while the cluster system is showing the weakest memory effect with the strongest interaction strength. From the above observations, it can be concluded that FC memory effect is independent of the type of dipolar interaction (positive or negative) present in the system, but only dependent on the resultant strength of dipolar interaction. On the other, it can be postulated that like coercivity, degree of partial alignment is not likely to effect on the FC memory effect in a system of superparamagnetic nanoparticles.

2.8 Anisotropy related to interparticle interaction

The anisotropy constants have been calculated from the values of saturation magnetization M_s and the size of the nanoparticles using the equation (11).

$$K_o = \frac{2M_o}{2\beta M_s V} \ln(2\beta M_s H_o V), \quad \beta = \frac{1}{K_B T} \quad (11)$$

Since, the saturation magnetization is independent of interparticle interaction, so the calculated anisotropy is considered as the anisotropy contributed from the size only. Also for the three systems, it should be same as the size is retained same. The obtained values of anisotropies are shown in the table 2. The order of the calculated anisotropy value is obtained one order higher than that of the bulk value which is obvious due to the surface effect. It is worth mentioning that

the primitive particles in all three systems are same, so the anisotropy contributed from the similar average size should be same in all three cases. But at the same time, the effects of both size and interparticle interaction should be reflected on the measured blocking temperature from Kneller plot. Thus, T_B can be written as

$$T_B = T_{Bo} + T_{int} \quad (12)$$

where, T_{Bo} and T_{int} are blocking temperatures contributed from the size and interparticle interaction respectively. If V is the average volume of the iron oxide nanoparticles, then it can be related to the anisotropy K_o as

$$K_o V = 25k_B T_{Bo} \quad (13)$$

Combining equations (12) and (13), T_{int} is obtained and hence respective interaction energies. Calculated parameters are shown in the table 3. T_{int} and E_{in} are found maximum for the aggregate system, while for the cluster system these are observed negative. The negative value here interprets that the anisotropy energy for the cluster system is even less than the primitive system. This is due to the random orientation of magnetic easy axes in the cluster system, where even after having the smaller interparticle spacing than the assembly system, it shows the lowest anisotropy energy.

System	T_B (K)		K_o (Jm^{-3})	T_{Bo} (K)	T_{in} (K)	E_{in} (J)
	From Kneller plots	From M-T				
IO _{NPs} @OA	123	90	3.7×10^5	70.75	37.75	52.11×10^{-23}
IO _{agg} @CTAB	126	127	-	-	77.62	77.62×10^{-23}
IO _{NPCs} @PAA	109	52	-	-	-18.75	-25.87×10^{-23}

Table 3. Table of blocking temperature, anisotropy constant and anisotropy energy of the three systems of nanoparticles.

3. Conclusion

In conclusion, the variation in the spatial ordering and magnetic easy axis orientation is realized to be responsible for the observed anomaly in dipolar interaction. These also result in the observed variation in coercivity and remanence for the aggregate and the cluster systems. The observed characteristics are found to be related to the relative broadening of anisotropy energy barrier distributions. The trend of blocking temperature is quite interesting for the three systems

as the cluster system shows the lowest blocking temperature even after having the strongest dipolar interaction. This is relevant to the fastest spin relaxation fascinated by the strongest demagnetizing interaction. FC memory effect is observed to be independent of the relative strengths of the magnetizing or demagnetizing type of interaction, but dependent only on the resultant dipolar interaction. The organization dependent anomalous behaviour of magnetic nanoparticles assembly, in this study, will open up new prospective for achieving extraordinary collective magnetic properties of secondary nanosystems and hence superior technological efficiency.

C. Controlled secondary growth of CoFe_2O_4 nanoparticles to achieve hierarchical assembly structure

1. Introduction

Hierarchical assembly formation of magnetic nanoparticles has been emerged as a promising bottom up approach for achieving the next generation of functional materials [17]. A few works on the hierarchical assembly formation of magnetic nanoparticles can be found in the literatures. Polyol method was used to develop spherical assemblies of magnetite nanoparticles, where poly(vinylpyrrolidone) was shown to be responsible for the formation of such structures; however the complete formation mechanism was not fully realized [18, 19]. Role of π - π interaction among the primary magnetite nanoparticles in directing their uniform spherical assembly formation was studied, where magnetite nanoparticles were capped with 2-carboxyterthiophene (TTP-COOH) monolayer [20]. However, weak interaction among the particles in this assembly system was not adequate to make them stable in different conditions, prior to the applications. Binder effect of water molecules and the capping effect of alcohol groups over primary nanoparticles were shown to be responsible for the formation of Co_3O_4 iso-oriented spherical assemblies [21]. A ternary surfactant combination was found to act as the mortar for the formation of similar assemblies of magnetite nanoparticles in a solvothermal reduction reaction [22]. Functional polystyrene was also investigated as the mortar for magnetic nanoparticles assemblies. Iso-oriented assemblies of CoFe_2O_4 with both spherical and cubical structures were developed based on a boiling bursts technique on a high-boiling point solvent by periodic injection of hexane utilizing a mixed metal oleate precursor [23]. A normal micelles route using sodium dodecylsulfate (SDS) as surfactant was also used to form spherical secondary structure [24].

Here, oleic acid, an unsaturated fatty acid has been used for achieving hierarchical assemblies of cobalt ferrite nanoparticles. The used synthesis method is a modified co-precipitation route, where, the addition of an extremely polar solvent, Dimethyl sulfoxide (DMSO) with water made the oleic acid miscible in the reaction. The concentration of oleic acid is varied systemically so as to understand how oleic acid can control the growth of the primary particles and their subsequent aggregation behaviour to form hierarchical assemblies. Moreover, the importance of DMSO in obtaining spherical assemblies has been explained. Structural information obtained from the SAXS (Small- angle X-ray scattering) have been used along with direct evidences obtained from TEM (Transmission Electron Microscopy) to probe different length scales and to reveal the nature of interparticle correlations in all the developed systems. Observed morphological characteristics of the hierarchical assembly system are also corroborated to its collective magnetic properties.

2. Results and discussion

2.1 Hierarchical assemblies of CoFe_2O_4

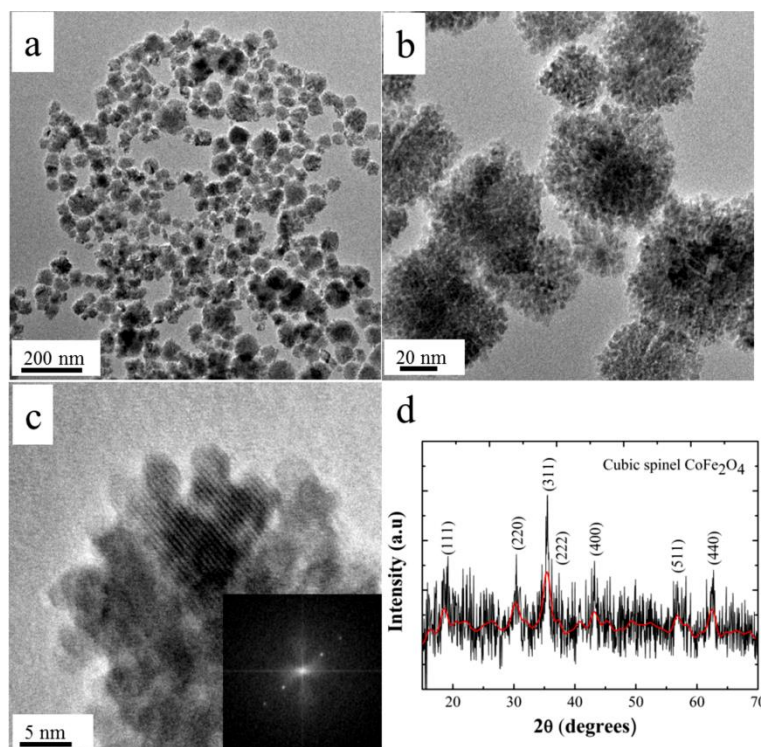


Fig. 1 CoFe_2O_4 hierarchical assemblies obtained with 0.14 M of oleic acid: (a) TEM image (scale is 200 nm), (b & c) HRTEM (scales are 20 nm and 5 nm respectively) and (d) shows the XRD pattern (Red lines show the FFT filter smoothing).

The powder sample prepared with 0.14 M oleic acid has been characterized with Transmission electron microscopy (TEM) and X-ray diffraction technique (XRD) for knowing the developed microstructure and crystalline phase respectively. In the Fig.1, TEM images show the formation of nearly spherical assemblies with average size 50 ± 3 nm (Fig. 1a). High magnification images (Fig.1b and c) show that the primary particles of average size 5 ± 1 nm are aggregated in iso-oriented manner inside the assemblies. The iso-orientations of the primary particles are further confirmed from the related FFT image, which shows symmetrical aligned spots like satellite reflections due to double diffraction (shown in the inset of Fig.1c). Moreover, from the further magnified image it is observed that shapes of the primary particles are not uniformly spherical, and the neighboring particles have shared their edges to form interconnected structures. Fig. 1d shows the diffraction pattern of the assembly system, where the observed Bragg reflection peaks can be indexed to CoFe_2O_4 with cubic spinel structure (JCPDS 22-1086) on the basis of their positions and relative intensities. Absence of any other phase-related peaks implies that obtained assemblies are purely of CoFe_2O_4 cubic spinel structure. This also means that there is no intermediate hydroxide state in these assemblies. The average crystallite size was estimated

using Single line analysis considering the most prominent peak (311) and found to be 7.6 nm. The observed higher value of crystallite size than the average size of the primary particles obtained from TEM is not surprising, because this is consistent with the observations obtained from FFT and HRTEM, where the primary particles are shown to be connected and oriented in same crystallographic directions inside the individual assembly.

2.2 Effect of oleic acid concentration

CoFe₂O₄ assemblies were synthesized using an oxidative precipitation method, where, DMSO acts as the oxidizing agent to oxidize Fe²⁺ to Fe³⁺. Moreover, due to the high miscibility of DMSO with oleic acid, nucleation and growth of the nanoparticles were expected to be occurred in a salt-surfactant homogenous condition. Since, the oxidation potential of Co²⁺ is much lower than that of Fe²⁺, so Co²⁺ remains same in the reaction. It is worth mentionable here that the use of the ferrous salt over ferric salt is advantageous as the oxidation of Fe²⁺ (unstable state) to Fe³⁺ (stable state) results excess Gibbs free energy, which favours the growth of crystalline cobalt ferrite at low temperature and at short reaction time. As mentioned in the synthesis, the similar reaction procedures were followed for other two extreme cases also, where, the only difference was the concentration of oleic acid. These two samples have also shown the formation of the cubic spinel CoFe₂O₄ phase. However, TEM images show some interesting differences of these two systems from the assembly system in terms of both primary particles' size and their aggregation behaviour. It is found that the sample CF1, prepared with the lowest concentration of oleic acid (0.07 M) consists of irregular shaped nanoparticles of average size 40 ± 5 nm with uncontrolled agglomeration behaviour and the last sample CF3, prepared with the highest concentration of oleic acid (0.21 M) shows basically some separated nanoparticles of average size 6 ± 2 nm. In this sample also, along with the separated particles few spherical aggregates are observed. The microstructure obtained for the CF1 sample is not so surprising, because uncontrolled growth and agglomeration of the magnetic nanoparticles can be happened at very low concentration of surfactant. However, the obtained microstructural similarity of CF2 and CF3 systems, i.e., the similar spherical aggregation behaviour in both the systems (shown in the Fig. 2b and c) is interesting and can reveal the formation mechanism of the hierarchical assembly. But, before going to that all the length scales obtained from the TEM images

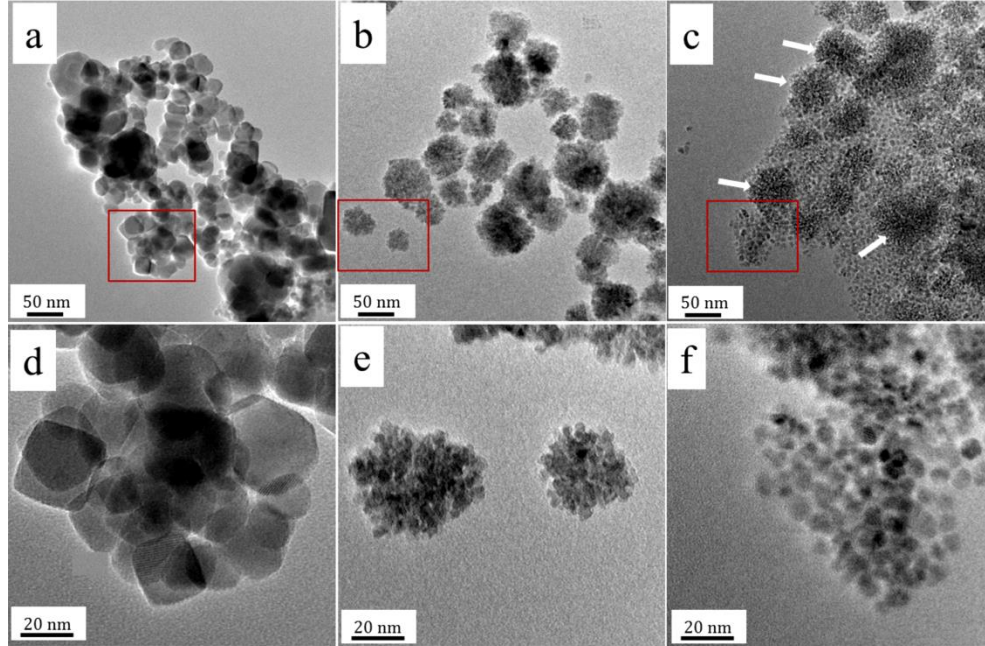


Fig. 2 TEM images of CoFe_2O_4 nanosystems prepared with three concentrations of oleic acid (a & d) 0.07 M, (b & e) 0.14 M and (c & f) 0.21 M. In the Figure c, white arrows are guide to the eye, showing the quasi-formation state of hierarchical assemblies.

have been further confirmed using SAXS technique. From the SAXS profiles (shown in the Figure 3), it is apparent that, although the functionality of low q region ($\sim 0.1\text{-}0.5 \text{ nm}^{-1}$) remains almost identical for CF1 and CF3, there exists significant differences in the functionality in the higher q regime (~ 0.5 to 1 nm^{-1}). The variation in the higher q regime manifests due to the differences in basic size and the nature of interparticle correlation of the particles in three systems. It is discernible that the overall functionality of the scattering profile of CF2 and, in particular, its slope in low q regime ($\sim 0.1\text{-}0.5 \text{ nm}^{-1}$) is distinctly different than that of either in case of CF1 or for CF3. The effective scattering intensity in all the three systems can be considered as cumulative scattering contributions from two components i.e., $I(q) = I_1(q) + I_2(q)$, where, $I_1(q)$ is the scattering contribution from the agglomerated particles and $I_2(q)$ is the scattering contribution from oleic acid molecules present in the samples. Now, $I_1(q)$ can be approximated as

$$I_1(q) = C \int_0^{\infty} P(q, R) v^2(R) D(R) S(q, R) dR \quad \dots\dots\dots (3)$$

Assuming spherical shape of the particles with radius R , the form factor $P(q, R)$ is expressed as

$$P(q, R) = 9 [\sin(qR) - qR \cos(qR)]^2 / (qR)^6 \quad \dots\dots\dots (4)$$

where, C is a scale factor that depends on scattering contrast and number density of the particles but is independent of q . $v(R)$ is the volume of a particle with radius R .

$D(R)$ represents the particle size distribution and assumed to be log-normal

$$D(R) = \frac{1}{\sigma R \sqrt{2\pi}} \exp \left[-\frac{(\ln(R/R_0))^2}{2\sigma^2} \right] \dots\dots\dots (5)$$

S(q, R) represents interparticle structure factor. A fractal like structure-factor with fractal dimension, D, monomer radius of the monomer, x, cut-off function h(r, ξ) with cut-off length ξ of fractal correlation were considered and is expressed as

$$S(q, x) = 1 + \frac{D}{x^D} \int_0^\infty R^{D-3} h(r, \xi) \frac{\sin(qr)}{(qr)} r^2 dr \dots\dots\dots (6)$$

with exponential cut-off function, $h_{Exp}(r, \xi) = \exp \left[-\left(\frac{r}{\xi}\right)^1 \right] \dots\dots\dots (7)$

For the other scattering contribution, I₂(q), similar equations have been considered, but without any structure-factor.

Scattering patterns of CF1 and CF2 have been well fitted using fractal like structure factor. However, but for CF3, the peak-like feature around q= 0.8 nm⁻¹ in the scattering profile could be explained only by consideration of hard sphere type structure factor [25]

$$S(q, R_{hs}) = \frac{1}{\left(1 + \frac{24\phi G(2qR_{hs}, \phi)}{2qR_{hs}} \right)} \dots\dots\dots (8)$$

G(X) depends on volume fraction (φ) and hard sphere radius (R_{hs}).

Table. 1 listed the obtained length scales from these fittings, which show a good agreement with the particle/cluster sizes estimated from TEM images.

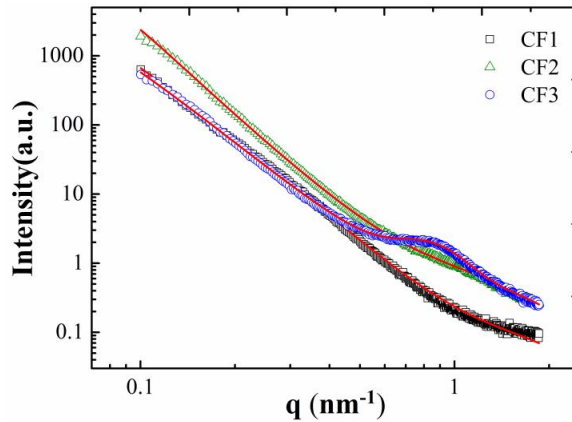


Fig. 3 SAXS profiles in double logarithmic scale (solid lines represent the fitted curves) of the three systems.

Table 1. Table showing estimated crystallite sizes and related micro strains from XRD, also primary and secondary particle sizes from TEM and SAXS.

System	$\langle D_{XRD} \rangle$ (nm)	Microstrain	Primary particle size (nm)		Secondary particle size (nm)	
			$\langle D_{TEM} \rangle$	Median size (R_0) from SAXS	$\langle D_{TEM} \rangle$	Median size (R_0) from SAXS
CF1	8.6	0.0105	40 ± 5	32.0	-	-
CF2	7.6	0.0109	5 ± 1	3.4	50 ± 10	49.0
CF3	3.2	0.0267	6 ± 2	6.4	-	-

Based on the above microstructural observations it is understood that the concentration of oleic acid is crucial for achieving the hierarchical assemblies. Therefore, to identify the nature of oleic acid binding to the nanoparticle surface and to quantify the amount adsorbed oleic acid at different concentrations FTIR and TGA analysis were performed. Fig. 4a shows the comparative FTIR plots of the three systems. The common peak observed at 1630 cm^{-1} for all three samples corresponds to the H-O-H scissoring from free or adsorbed water molecules. The intense absorption peaks around 578 cm^{-1} for all three samples are attributed to Fe-O or Co-O vibrations. The absence of characteristic C=O stretching vibration peak around 1700 cm^{-1} in the Fig.4a FTIR spectra witnesses the lack of pure, unmodified oleic acid in all the three nanopowders. Instead of this, two new peaks have appeared at 1569 cm^{-1} and 1415 cm^{-1} , corresponding to asymmetric and symmetric COO^- stretching vibrations respectively. However, both of these two peaks are observed to be distinct for the CF3 sample only. The obtained separation ($\Delta=154 \text{ cm}^{-1}$) between these two peaks corresponds to the bridging bidentate type of interaction of COO^- with the nanoparticles' surface metal atoms (Fe and Co). For CF1 and CF2, though the COO^- symmetric stretching peak is observed distinctly, the asymmetric peak is observed as a weak shoulder peak. This signifies that in CF3 sample only, oleic acid molecules are effectively bonded to the nanoparticles surface, which could be justified as the consequence of higher oleic acid concentration used in this sample. This is also supported by the higher intensities of CH_2 symmetric and asymmetric peaks at 2923 cm^{-1} and 2852 cm^{-1} respectively for this sample [30]. However, escaping this usual trend of intensity variation with oleic acid concentration, CF2, i.e. the assembly sample shows two highest intense peaks at 1115 cm^{-1} and 949 cm^{-1} , which are attributed to C-O stretching and out-of-plane O-H bending vibrations. Moreover, one additional peak is observed for this sample at 1482 cm^{-1} which is ascribed to the in-plane O-H bending vibrations. Thus, the observed intense peak of C-O stretching and O-H bending vibrations for the CF2 sample means that, there might be a fraction of oleic acid molecules which are in quasi-bonding state.

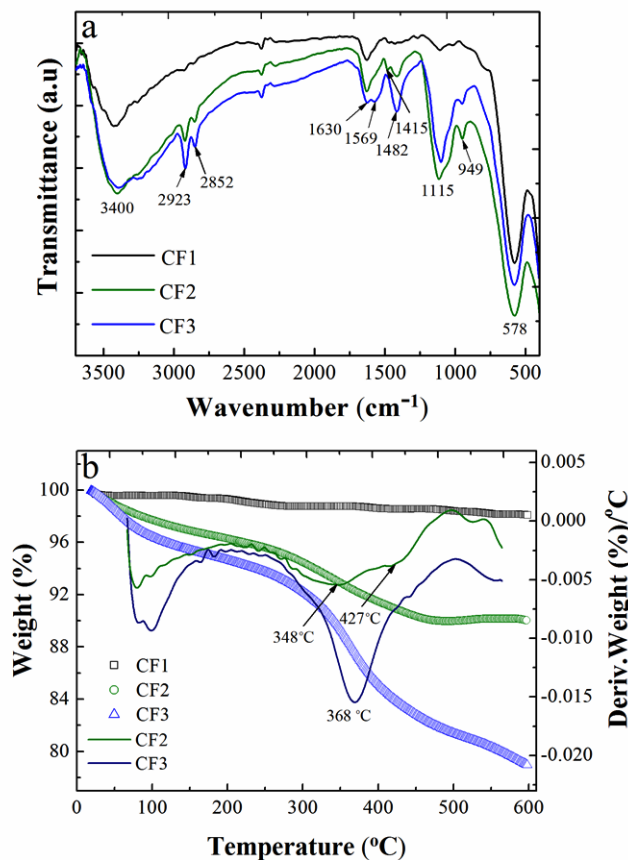


Fig. 4 Surface compositional analysis: (a) FT-IR spectra and (b) TGA of the CF1, CF2 and CF3 samples. Figure b also shows the DTG plots of the CF2 and CF3 samples.

The observed anomaly in FTIR can be further understood based on the TG analysis. Figure 4(b) shows the comparative TGA plots of the three systems. In the TGA plots, the CF1 sample shows significantly low weight loss ($\sim 2\%$), while for CF2 and CF3 samples around $\sim 11\%$ and $\sim 22\%$ of weight losses are obtained respectively. However, the TGA plots of CF2 and CF3 show respective $\sim 2\%$ and $\sim 3\%$ weight losses up to $100\text{ }^\circ\text{C}$ due to the removal of adsorbed water molecules. It is obvious to observe higher percentage of weight loss for the samples prepared with higher concentrations of oleic acid. It is also known that depending on the availability of oleic acid in the system, monolayer or bilayer can be formed over the nanoparticles. However, here, for none of the samples the formation of oleic acid bilayer was observed. This is supported by the absence of any characteristic peak of C=O stretching in the FTIR spectra. Oleic acid bilayer is usually formed through physisorption of oleic acid molecules over the first chemisorbed layer, where, the physisorbed oleic acid molecules possess the hydrophobic tails towards the first layer and the COOH groups remain undisturbed pointing outward from the nanoparticles surface. The derivative TGA plot of CF2 sample shows two step weight loss ($348\text{ }^\circ\text{C}$ and $427\text{ }^\circ\text{C}$), which again contradicts the affirmation based on the FTIR spectra interpretation that in these cases results only monolayers. But, it is not always true that only the bilayer can

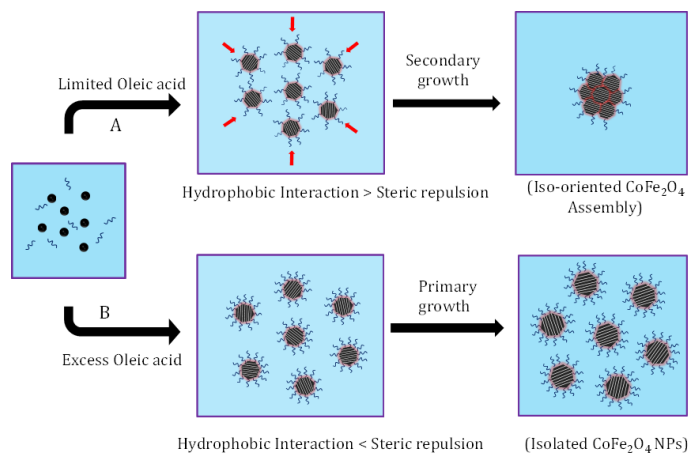
result two step weight losses in the temperature range (200°C - 600°C). Few reports are there showing the two step weight loss and the explanation was given as the possibility of two types of binding strength due to the chemisorption process itself. Another possible reason could be given as the contribution of the van der Waal interaction among the neighboring hydrophobic chains of the already chemisorbed oleic acid molecules in *cis* form. But, in that case the question is that why it will happen only for the CF2 sample. The CF3 sample which is uniformly capped by oleic acid should have higher probability for this type of van der Waal interaction among the chemisorbed molecules. Therefore, in the case of CF2 sample, the already mentioned explanation of dual binding strength can be put forwarded to interpret the DTG plot. If we see the first peak of CF2 sample, it is coming a little bit lower temperature than that of the single peak of CF3 sample. Moreover, this peak of CF2 sample is noticeably broad. This observation implies that in the CF2 sample a major fraction of oleic acid molecules are not chemisorbed uniformly and effectively over the particles like that of the CF3 sample. The possible reason behind this could be the secondary growth process of the particles in the CF2 sample. During this process oleic acid molecules can detach from the particles' surface at the interface regions. Straight way, it can be said that a fraction of oleic acid molecules is in quasi bonding state in this sample. The second peak which is coming at higher temperature (427 °C) could be due to the contribution of the fraction of effectively chemisorbed oleic acid molecules on the outer part of the clusters which is unaffected by the clustering process. The reason of higher inflection temperature is the smaller size of the primary particles in the CF2 sample, because binding affinity of capping molecules to smaller particles is enhanced as well as their binding strength. Quantification of oleic acid molecules per nanoparticle in the three systems and hence the number of oleic acid molecules per unit area of the nanoparticles could be interesting here. The obtained TGA weight losses are used to estimate the oleic acid molecules per nanoparticle using the following formula.

$$N = \frac{4\rho R^3 \pi w N_A}{3(100 - w)M_{OA}} \dots\dots\dots (9)$$

where, N is the number of oleic acid molecules per particle, w is the TGA weight loss (weight losses due to the adsorbed moisture was not accounted), N_A is the Avogadro number, ρ is the density of CoFe_2O_4 , R is the radius of nanoparticles (taken from SAXS fittings) and M is the molecular weight of oleic acid ($282.47 \text{ g mol}^{-1}$). Using this equation the number of oleic acid molecules per unit centimeter square of the nanoparticles' surface (N/A) are obtained as 0.356×10^{14} , 0.550×10^{14} and 2.24×10^{14} for the CF1, CF2 and CF3 samples respectively. It is not surprising to have such small value of N/A for the CF1 sample, but for the CF2, N/A is found to be of the same order that for CF1, which is surprising. Thus, the obtained smaller value of N/A for the CF2 sample even after having the highest surface-to-volume ratio (smallest primary particle size) again confirms the poor average packing density of oleic acid over the primary nanoparticles in the CF2 sample.

2.3 Formation mechanism of the hierarchical assemblies

From the above discussion, a plausible growth mechanism of the hierarchical assembly system can be proposed. It was already mentioned that the CF1 is an extreme condition, where the aggregation behavior of the particles is totally uncontrolled, is far from the assembly system. Thus, this system might not be relevant directly in understanding the formation mechanism of the hierarchical assembly system. However, at the first sight, comparing the microstructures of CF2 and CF3 samples (Fig.2) it can be understood that in the assembly system the interaction between primary particles are sufficiently strong to make them aggregated, which is not completely happening in the case of CF3. It is also observed that the size of the primary particles in the CF3 sample is higher than that in the assembly system (confirmed from the SAXS analysis and HRTEM images). But this is not usually observed in an ordinary surfactant controlled growth process, where the size of the nanoparticles is often observed to be decreasing with the increasing concentration of the surfactant. This implies that in the hierarchical assembly system the growth process is fully dominated by a secondary growth mechanism to form the iso-oriented structure, while in the CF3 sample, this is fully dominated by Ostwald ripening. It is now to be understood which factor is determining the domination of the different growth processes in these two systems. Then it will be helpful to reveal the formation mechanism of the hierarchical system. It is worthwhile to mention that the solvent of the synthesis for the development of CoFe_2O_4 nanoparticles was the mixture of DMSO and water which is a mixed polar solvent. Again, the formed primary particles are of hydrophobic nature due to the capping of oleic acid. Therefore, there is a strong possibility of the developed hydrophobic nanoparticles to be aggregated through the hydrophobic interaction to minimize the total interfacial surface area. The aggregation of the oleic acid molecules to dimer and multimer states due to the hydrophobic interaction among the alkyl chains and hydrogen bonding between COOH groups at the pre-nucleation stage of the nanoparticles cannot be neglected. However, addition of base TMAOH likely to dissociate these dimer or multimer of oleic acid molecules instantly, because at high pH deprotonated carboxylic groups repel each other and destabilize this type of aggregation state. As the nanoparticles are formed with hydrophobic tails of oleic acid projected outwards, the hydrophobic interaction among the particles becomes significant to make them aggregated. However, another factor, steric repulsion among them due to the capping effect should act at the same time to oppose the aggregation. But at a critical condition the hydrophobic interaction force can be dominating over the steric repulsion and then particles are bound to be aggregated and which is happened in the case of CF2 system. However, the process is not completed simply after the aggregation process and follows a subsequent secondary growth process, oriented attachment, to align the primary particles in same crystallographic direction. On the other hand, where the repulsion force is dominating over the interaction force they follow the same common primary growth process of individual particles, but in controlled fashion. The whole formation mechanism is depicted in the Scheme 1.



Scheme 1. Formation mechanism of the spherical assembly system: Path A shows the aggregation and subsequent oriented attachment processes, while the path B shows the domination of the primary growth process for resulting separated particles.

2.4 Raman spectroscopy and estimation of Co²⁺ distribution

Raman spectroscopy is a useful tool to reveal the cation distribution factor of a cubic spinel system, which is relevant to the magnetic properties of CoFe₂O₄. It is known that Co²⁺ has a non-zero orbital momentum and depending on the distribution of Co²⁺ at different interstitial sites, like tetrahedral and octahedral the magnetic properties of the material can be varied, which is very much dependent on the preparation methods of the material. Therefore, it is important to check the values of the cation distribution factor for all the three CoFe₂O₄ samples before trying to understand their magnetic properties in terms of primary particle size and their aggregation behaviour. Raman spectroscopy can give information related to the structural disorder and developed strain in the system. A stoichiometric cobalt ferrite has a cubic inverse spinel structure, where, all the divalent cations (Co²⁺) occupy the octahedral sites (B) and all the trivalent cations (Fe³⁺) occupy both the tetrahedral sites (A) and octahedral sites in equal proportion. The cubic spinel structure belongs to the space group Fd $\bar{3}$ m, for which group theory predicts the following modes.

$$\Gamma = A_{1g}(R) + E_g(R) + F_{1g} + 3F_{2g}(R) + A_{2u} + 2E_u + 4F_{1u}(IR) + 2F_{2u} \dots \dots \dots (10)$$

where, the A_{1g} , E_g and $3F_{2g}$ modes are Raman active, the $4F_{1u}$ modes are IR active and the F_{1g} , A_{2u} , $2E_u$ and $2F_{2u}$ modes are silent. The A_{1g} represents the symmetric stretching of oxygen atoms with respect to the metal ions located at tetrahedral sites and the E_g and $3F_{2g}$ modes represent the symmetric and asymmetric stretching vibrations of oxygen with respect to the metal cations present at the octahedral sites. Three systems show all these characteristics five Raman modes at respective positions (shown in the Fig.5). The fitted spectra also show some extra peaks, which might be obtained due to the symmetry breaking at nanosize. Positions and area of different peaks have been obtained by deconvolution of the spectra with Lorentzian function.

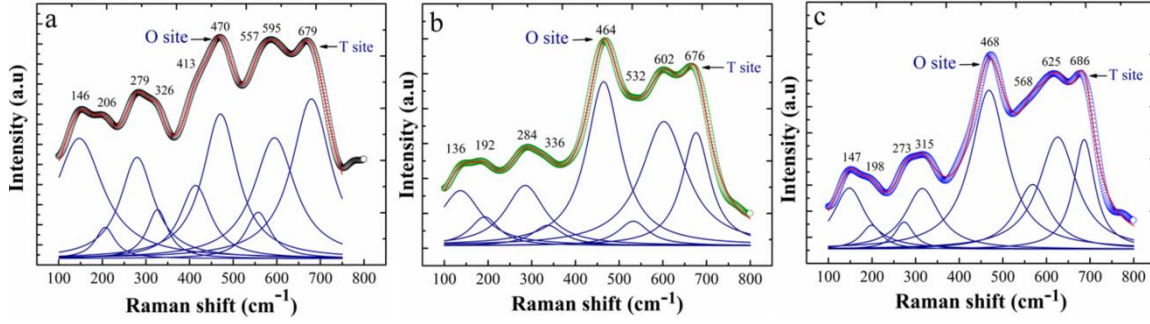


Fig. 5 Raman spectra of the samples CF1 (a), CF2 (b) and CF3(c). Red lines show the fitted spectra and Lorentzian deconvolutions show the positions of different vibration modes.

The peak around $\sim 192\text{-}206\text{ cm}^{-1}$ is attributed to the $F_{2g}(1)$ mode, the peak around $\sim 273\text{-}284\text{ cm}^{-1}$ and $\sim 315\text{-}336\text{ cm}^{-1}$ represent the E_g mode, the peaks around $\sim 464\text{-}470\text{ cm}^{-1}$ and $\sim 532\text{-}568\text{ cm}^{-1}$ are attributed to the $F_{2g}(2)$ and $F_{2g}(3)$ modes respectively, while the high frequency peaks at $\sim 595\text{-}625\text{ cm}^{-1}$ and $\sim 676\text{-}686\text{ cm}^{-1}$ represent the A_{1g} mode. Comparing the vibration frequencies of Fe-O and Co-O, it can be confirmed that the peak centred around $\sim 595\text{-}625\text{ cm}^{-1}$ can be assigned to (Co-O) A_{1g} mode, while the peak centred around $\sim 676\text{-}686\text{ cm}^{-1}$ can be assigned to (Fe-O) A_{1g} mode. The intensities of these two peaks with A_{1g} modes can be used to estimate the cation distribution factor. The cation distribution factor (δ) occasionally illustrates the fraction of Co^{2+} at tetrahedral site, and in this case the structure can be written as $(\text{Co}_{\delta}^{2+} \text{Fe}_{1-\delta}^{3+})_A [\text{Co}_{1-\delta}^{2+} \text{Fe}_{1+\delta}^{3+}]_B$. From Raman spectra, δ can be calculated by using the equation (11).

$$\delta_{Raman}^A = \frac{I_{Co}}{2(I_{Co} + RI_{Fe})} \quad (11)$$

where, I_{Co} and I_{Fe} are the intensities of A_{1g} (Co-O) mode and A_{1g} (Fe-O) mode respectively. This equation was first employed for the calculation of cation distribution factor in $\text{Mg}_x\text{Fe}_{3-x}\text{O}_4$ nanoparticles, where, a satisfactory agreement was observed between the estimations obtained from Raman data and Mossbauer data for the empirical value of $R = 0.5$. Using the same equation and the R value 0.5, here also, δ is estimated as 0.35, 0.26 and 0.26 for CF1, CF2 and CF3 respectively. Thus, it is observed that the fractional occupancy of tetrahedral sites with Co^{2+} is significantly higher for the biggest particles system prepared with the least concentration of oleic acid, while for the assembly and other extreme system, it is found to be small and similar. Thus, it can be concluded that the concentration of oleic acid can influence the cation distribution of the cobalt ferrite nanoparticles, if the concentration is significantly low and results in uncontrolled growth of the particles. Otherwise, above an optimum level of oleic acid concentration, where the growth process is fully controlled, irrespective of the type of growth processes (i.e., dominantly Ostwald ripening or oriented attachment), concentration of oleic acid

does not affect on the cation distribution factor. It is also observed that all the peaks for CF2 sample are red-shifted with respect to the respective peaks of CF1 and again blue shifted for the CF3 sample. The observed red-shifting for the CF2 sample can be related to the produced crystal disorder during fusion process among the primary particles, while the blue-shifting for the CF3 sample could be related to the induced strain at the surface of the nanoparticles due to the higher density of covalent bonding between oleic acid and nanoparticles surface cations. Induced higher strain in the CF3 system is also confirmed from the estimated higher value of microstrain in the single line analysis of the XRD data (Table 1).

2.5 Magnetic properties

Fig.6 shows the comparative field dependent magnetization (M-H) plots of all the three systems at room temperature. It is observed that the M-H plot for the CF1 sample shows the hysteresis behavior, which corresponds to the prevalence of the long-range magnetic ordering in this system. The observed hysteresis behavior at room temperature for this system is an obvious effect of the bigger particle size. Unlike this sample, CF2 and CF3 show superparamagnetic like M-H plots, but still coercivity values are non-vanishing. The room temperature coercivity values of the three samples have shown a decreasing trend with the increasing concentration of oleic acid. However, this decreasing trend is not due to any monotonous dependency of decreasing particle size, because, HRTEM and SAXS results have already shown that the size of the primary particles in the assembly system is smaller than that in the CF3 sample. In this situation, the observed higher value of coercivity for the hierarchical assembly system as compared to the CF3 sample could be related to the induced anisotropy due to the strong interparticle interaction in this system. Like the coercivity, reduced remanence values obtained at room temperature also show the same trend and this can be explained on the basis of same argument, i.e. stronger interparticle interaction in the assembly system. However, the low temperature coercivity values have not shown the similar trend that observed at room temperature measurements. It is observed that CF3 sample exhibits significantly higher coercivity value (7.0 kOe) as compared to the assembly system (3.9 kOe) at 5K. This enhancement cannot be due to the intrinsic size effect (i.e., bigger size of the primary particles) or interparticle interaction effect (i.e., weaker interparticle interaction due to higher interparticle spacing), because, if it is due to either of them, then the same trend should be observed at room temperature measurement also. This observed enhancement of coercivity only at low temperature reflects the existence of the low temperature spin glassy state in the CF3 system and here it could be possible due to the developed surface strain by effective oleic acid capping over the primary particles. The possibility of induced surface strain in this system has been already confirmed by the Raman spectroscopy. Saturation magnetization values of all the three systems have been obtained close to the bulk saturation magnetization value of CoFe_2O_4 , however there is small differences among the three systems. Observed slightly smaller value of M_s for the assembly system could be related to the interfacial disorders among the primary particles.

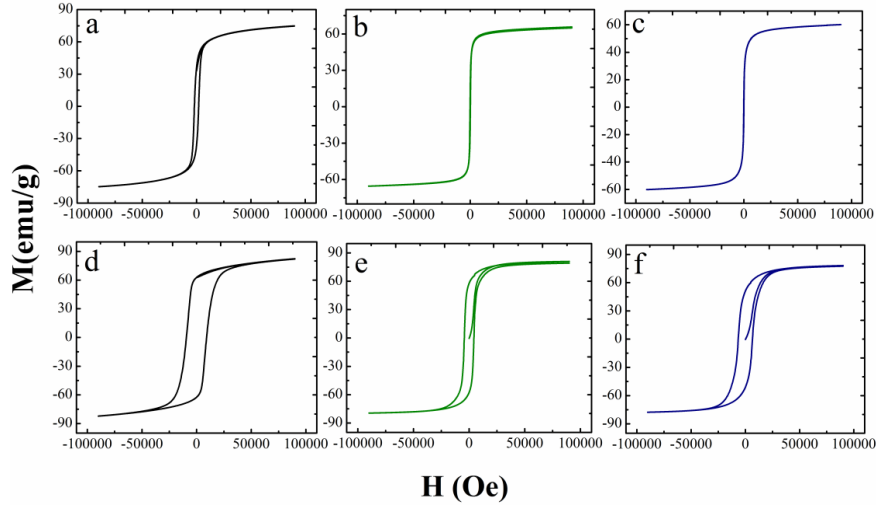


Fig.6 Room temperature and low temperature M-H plots of CF1 (panel a and d respectively), CF2 (panel b and e respectively) and CF3 (panel c and f).

M-T plots performed with ZFC and FC conditions are shown in the Fig.7. It is observed that for the CF1 sample ZFC and FC curves are not coinciding even at 300 K, signifying the high effective anisotropy, which is obvious for this sample because of the bigger particle size 30-40 nm. However, for CF2 and CF3 samples, blocking temperatures have been observed below the room temperature with the lowest value for CF3. Observed higher value of the blocking temperature for the assembly system even after having the smaller primary particle size in comparison to the CF3 sample again implies the effect of strong interparticle interaction among the primary particles in the assembly system. Most importantly, the M-T measurements have shown that the moment/g values in the FC curve for the assembly sample are comparatively high and which signifies the higher magnetic tracking capability of this system.

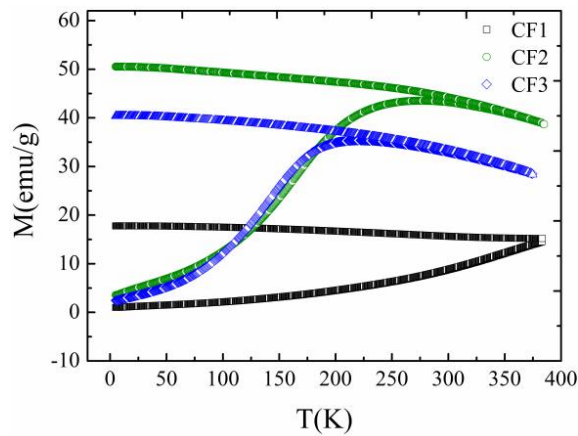


Fig.7 Comparative M-T plots of the three systems with applied probe field 1000 Oe.

3. Conclusions

In the summary, we presented a novel concept on the formation of hierarchical assemblies of CoFe_2O_4 nanoparticles using oleic acid as the structure directing agent. Results show that the concentration of oleic acid is the critical parameter in controlling the stability of the primary nanoparticles and which eventually leads to the formation of hierarchical assembly structures. Stability of the primary particles determines the nature of dominant growth processes, i.e. growth of the primary particles or secondary growth among the particles to give different organization states of the nanoparticles. When the concentration is very low, the growth of the primary particles is completely uncontrolled and there is no possibility of subsequent secondary growth. On the other hand, when the concentration of oleic acid is very high, the developed primary particles are formed with adequate stability and due to that they also do not prefer a secondary growth process. However, at an intermediate critical concentration oleic acid capping is not so effective to make the particles separated from each other and push them to a secondary growth step, oriented attachment, yielding the hierarchical assemblies. It is identified that the dominant hydrophobic interaction over steric repulsion among the primary particles is the driving force to make the spherical aggregates of the particles at first and subsequently resulting in the hierarchical structures. From the concentration variation study, it is realized that both the growth processes, i.e. Ostwald ripening and oriented attachment cannot be effective at the same time. It is also observed that Co^{2+} distribution factor is independent of the type of growth processes, primary or secondary, but could be affected when much lower concentration of oleic acid is used, resulting uncontrolled growth of the particles. The effect of ordered structure of the hierarchical assembly system is reflected on the magnetic properties, like high magnetic moment, moderate coercivity etc. The stability mediated differential growth behavior of the CoFe_2O_4 nanoparticles in this study is opening up a new direction to design hierarchical ordered structures in desired ways to harness their advanced functionalities.

References

- [1] S. Kralj and D. Makovec, *ACS Nano* 2015, **9** (10), 9700.
- [2] D. Corato, et al. *ACS Nano* 2011, **5** (2), 1109.
- [3] R. Erb, et al. *Nature* 2009, **457**, 999.
- [4] N. Griffete, et al. *Chem. Commun.* 2012, **48** (92), 11364.
- [5] S. Ramesh, et al. *J. Mater. Res.* 2000, **15** (4), 944.
- [6] M. Ocaña, et al. *J. Colloid Interface Sci.* 2006, **294** (2), 355.
- [7] Y. Zhu, et al. *Colloids Surf. A Physicochem. Eng. Aspects* 2003, **231** (1-3), 123.
- [8] O. Chen, et al. *Nature Comm.* 2014, **5** (5093), 1.
- [9] W. Zhao, et al. *J. Am. Chem. Soc.* 2005, **127** (25), 8916.
- [10] J.L. Dormann, L. Bessais, D. Fiorani, *J. Phys. C: Solid State Phys.*, 1988, **21**, 2015.
- [11] J.L. Dormann, D. Fiorani, E. Tronc, *J. Magn. Magn. Mater.*, 1999, **202**, 25.
- [12] M. El-Hilo, K. O. Grady, and R. W. Chantrell, *J. Magn. Magn. Mater.*, 1992, **114**, 295.
- [13] K. Hiroi, K. Komatsu, and T. Sato, *Phys. Rev. B*, 2011, **83**, 224423.
- [14] J. S. Lee, R. P. Tan, J. H. Wu, and Y. K. Kim, *Appl. Phys. Lett.*, 2011, **99**, 062506.
- [15] V. M. Kalita, A. A. Timopheev, and S. M. Ryabchenko, *J. Exp. Theor. Phys.*, 2011, **112**, 441.
- [16] M. Thakur, M. Pal Chowdhury, S. Majumdar and S. Giri, *Nanotechnology*, 2008, **19**, 045706.
- [17] A. H. Groschel et al. *Nature* 2013, 503, 247.
- [18] K. Bhattacharya and P. Deb, *Dalton Trans.* 2015, **44**, 9221.
- [19] Y. Zhu et al. *J. Phys. Chem. C* 2007, **111**, 5281.
- [20] J. Jin et al. *Angew. Chem.* 2001, **40**, 2135.
- [21] T. He et al. *Chem. Mater.* 2004, **16**, 737.
- [22] Y. Hou et al. *Eur. J. Inorg. Chem.* 2004, **2004**, 1169.
- [23] N. Bao et al. *J. Am. Chem. Soc.*, 2009, **131**, 12900.
- [24] C. Cannas, et al. *Interface Sci.*, 2010, **343**, 415.

Outcomes of the project

List of Publications

1. M. Gogoi, P. Deb, D. Sen, S. Mazumder and A. Kostka, Enhanced Quantum Confined Stark Effect in a mesoporous hybrid multifunctional system, **Solid State Commun.**, 187 (2014) 48-52.
2. K. Saikia, D. Sen, S. Mazumder, P. Deb, Reassembling nanometric magnetic subunits into secondary nanostructures with controlled interparticle spacing **RSC Advances**, 5 (2015), 694-705.
3. K. Saikia, S.D. Kaushik, D. Sen, S. Mazumder, P. Deb, Fatty acid as structure directing agent for controlled secondary growth of CoFe_2O_4 nanoparticles to achieve mesoscale assemblies: A facile approach for developing hierarchical structures, **App. Surf. Sci.**, 379 (2016), 530-539.
4. K. Saikia, D.D. Sarma, P. Deb, Organization dependent collective magnetic properties of secondary nanostructures with differential spatial ordering and magnetic easy axis orientation, **J. Magn. Magn. Mater.** 408 (2016), 127-136.
5. K. Saikia, P. Deb, S.D. Kaushik and D. Sen, Solvent evaporation induced dense assembly of magnetic nanoparticles on Mesoporous silica spheres, (**Communicated**)

Patents

1. Magnetic secondary nanostructure as contrast agent for Magnetic resonance imaging (Application No. 201731009379)

Poster presented at Conferences

1. K. Saikia, S.D. Kaushik, D. Sen, S. Mazumder, P. Deb, Dense assembly of magnetic nanoparticles in correlated porous network of mesoporous silica for high performance MRI contrast agent (Presented in **6th Conference on Neutron Scattering November 21-23, 2016 at Bhabha Atomic Research Centre, Mumbai, India**)
2. K. Saikia and P. Deb, Modulation of collective magnetic properties of magnetic assemblies by varying organization structure (Presented in **Frontiers in Advanced Materials during June 15-18, 2015, IISc, Bangalore, India**).

3. K. Saikia, D. Sen, S. Mazumder and P. Deb, Secondary magnetic nanostructure developed through reassembly of subunits with controlled interparticle spacing: A small angle scattering study (Presented in **5th Conference on Neutron Scattering February 2-4, 2015, Homi Bhabha Centre for Science Education, Mumbai**).
4. K. Saikia, D. Sen, S. Mazumder, P. Deb, Study on the interparticle interaction of superparamagnetic iron oxide nanoparticles (Presented in **National Magnetic Resonance Society Symposium (NMRS-2014), February 2-5, 2014, Tezpur University, Tezpur**).

Achievements

1. **Best poster presentation award** from Neutron Society of India at **5th Conference on Neutron scattering (CNS-2016)** held at Homi Bhabha Centre for Science Education, Mumbai, India during 2-5th February, 2015

Ph.D. awarded

1. The project fellow **Mr. Koushik Saikia** of this project has defended his Ph.D. on 23.12.2016. The title of the thesis is '**Controlled Self-organization of Magnetic Nanoparticles and Their Collective Magnetic Properties Study**' under the supervision of Prof. P. Deb, Department of Physics, Tezpur University & PI of the project.

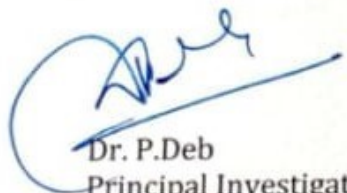
CONSOLIDATED STATEMENT OF ACCOUNTS

Sanction no. UDCSR/MUM/AO/CRS-M-186/12/508 Dated.27.11.2012.

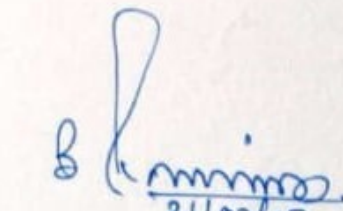
Project titled "Study on the controlled self assembly of magnetic nanostructures using neutron scattering"

Period : 1.4.2013 to 31.12.2016

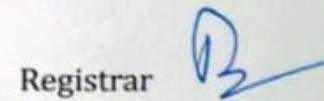
AMOUNT RECEIVED					AMOUNT SPENT					
Year	Manpower	Consumables	Contingency	Total	Year	Manpower	Consumables	Contingency	Total	Unspent balance
	Rs.	Rs.	Rs.	Rs.		Rs.	Rs.	Rs.	Rs.	(sl.5-10) Rs.
1	2	3	4	5	6	7	8	9	10	11
2013	168407.00	20000.00	15000.00	203407.00	2013	153097.00	10000.00	10000.00	173097.00	30310.00
2014	110690.00	10000.00	10000.00	130690.00	2014	168000.00	31011.00	16024.00	215035.00	(-)84345.00
2015	168000.00	20000.00	15000.00	203000.00	2015	109800.00	8989.00	17894.00	136683.00	66317.00
2016	192000.00	30000.00	15000.00	237000.00	2016	224000.00	13738.00	11544.00	249282.00	(-)12282.00
Total	639097.00	80000.00	55000.00	774097.00		654897.00	63738.00	55462.00	774097.00	NIL



Dr. P. Deb
Principal Investigator
UGC-DAE Project
Associate Professor
Dept. of Physics
Tezpur University



21/02/17
Finance Officer
Tezpur University
Finance Officer
Tezpur University



Registrar
Tezpur University
Registrar
Tezpur University

Principal Investigator
"Study on..... Scattering (SANS)
UGC-DAE Project
Dept. of Physics, Tezpur University

Statement of Accounts (4)

1. Name of the Principal Investigator : Dr. Pritam Deb
2. Department : Department of Physics, Tezpur University
3. UGC-DAE CSR Approval No. : No. UDCSR/MUM/AO/CRS-186/2015/067 Dated.7.5.2015

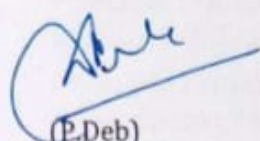
For 4TH Year (2016)

4. Title of CRS : Study on the controlled self assembly of magnetic nanostructures using neutron scattering
5. Effective date of starting of the CRS : 01.01.2013
6. Period of Expenditure : 01.12.2015 to 31.12.2016
7. Project Fellow : Mr. Kaushik Saikia
8. Details of Expenditure (Year Wise) : 2016

Sl. No.	Head	Amount Sanctioned & received in Rs.	Previous year expenditure 2015 (April - Nov) Rs.	Balance Rs.	Expenditure Incurred in Rs. 2015-16 (Dec2015- Dec, 2016)	Balance Rs.
1.	Fellowship	192000.00	109800.00	16200.00	224000.00	(-)15800.00
2.	HRA on fellowship	0.00	0.00	0.00	0.00	0.00
3.	Chemicals/Consumables	30000.00	8989.00	0.00	13738.00	16262.00
4.	Contingency	15000.00	17894.00	(-)3918.00	11544.00	(-)462.00
Total Rs.		237000.00	136683.00	12282.00	249282.00	0.00
Balance Rs.						0.00

(If Project Fellow is appointed than Sl No. 1)

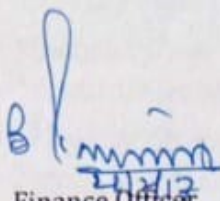
1. It is certified that the appointment has been made in accordance with the terms and the conditions laid down by the UGC-DAE-CSR.
2. If, as a result of check or audit objective, some irregularity is noticed later date, action will be taken to refund, adjust or regularize the objected amounts.



(P. Deb)
Principal Investigator
UGC-DAE CSR-M-186
Associate Professor
Department of Physics
Tezpur University

Principal Investigator

"Study on..... Scattering (SANS)
UGC-DAE Project
Dept. of Physics, Tezpur University



Finance Officer
Tezpur University
Finance Officer
Tezpur University



Registrar
Tezpur University
Registrar
Tezpur University



तेजपुर विश्वविद्यालय

(केंद्रीय विश्वविद्यालय)

नपाम, तेजपुर - 784 028, असम, भारत

TEZPUR UNIVERSITY

(A Central University)

Napaam, Tezpur - 784 028, Assam, India

Utilization Certificate (4)

Certificate (4)

Certified that the grant for **Rs.2,37,000.00 (Rs. two lakh thirty seven thousand only)** received from UGC-DAE Consortium for Scientific Research, Mumbai Centre under the Collaborative Research Scheme (CRS) entitled "*Study on the controlled self assembly of magnetic nanostructures using neutron scattering*" vide letter No. UDCSR/MUM/AO/CRS-M-186 /2016/906 Dtd. 01.03.2016 has been utilized for the purpose for which it was sanctioned and in accordance with the terms and conditions laid down by the UGC-DAE-CSR and there is unspent balance of **Rs.0.00(NIL)** under the project.

(P. Deb)

Principal Investigator
UGC-DAE CRS-M-186
Associate Professor
Department of Physics
Tezpur University

Principal Investigator
"Study on..... Scattering (SANS)
UGC-DAE Project
Dept. of Physics, Tezpur University

21/04/17
Finance Officer
Tezpur University
Finance Officer
Tezpur University

Registrar
Tezpur University
Registrar
Tezpur University